A systematic experimental study of rapidly rotating spherical convection in water and liquid gallium.

Julien Aubert, Daniel Brito[1], Henri-Claude Nataf, Philippe Cardin and Jean-Paul Masson.

Laboratoire de Géophysique Interne et Tectonophysique, Observatoire des Sciences de l'Univers de Grenoble, BP 53X, 38041 Grenoble cedex 9, France.

Abstract: Results of finite-amplitude convection experiments in a rotating spherical shell are presented. Water (Prandtl number $P = 7$) and liquid gallium ($P = 0.027$) have been used as working fluids. In both liquids, convective velocities could be measured in the equatorial plane using an ultrasonic Doppler velocimetry technique. The parameter space has been systematically explored, for values of the Ekman and Rayleigh numbers $E > 7\ 10^{-7}$ and $Ra < 5\ 10^{9}$. Both measured convective velocity and zonal circulation are much higher in liquid gallium than in water. A scaling analysis is formulated, which shows that higher convective velocities are an effect of the low Prandtl number in liquid gallium, and that higher zonal flows can be explained through a Reynolds stress mechanism. The Reynolds numbers in gallium ($Re = 250 - 2000$) are higher indeed than in water ($Re = 25 - 250$). An inertial regime sets up at high Re, in which kinetic energy does not dissipate at the scale of convective eddies and is transferred up to the scale of the container, where it is dissipated through Ekman friction of zonal flow. This upwards energy transfer can be seen as an effect of quasigeostrophic turbulence. Applying the scaling relations to an hypothetic non-magnetic flow in the Earth's core yields Reynolds numbers of the order of 10^8, in fair agreement with values required for dynamo action, convective velocities of order 10^{-3} m/s, zonal flow of similar amplitude, and eddy scales as low as 10 km.

Keywords: Convection, Geodynamo, Core, Ultrasonic, velocimetry.

[1]Corresponding author: `Daniel.Brito@ujf-grenoble.fr`, fax. (00 33) 4 76 82 81 01

	Unit	Definition	water at 20^{o}C	liq. gallium at 30^{o}C	Earth's Core
ρ	kg/m^3	Mean density	1000	^{a}6095	$\approx 10^4$
ν	m^2/s	Kinematic viscosity	10^{-6}	$^a 2.95\ 10^{-7}$	$^c \approx 7\ 10^{-6}$
α	K^{-1}	Thermal expansivity	$2\ 10^{-4}$	$^b 1.26\ 10^{-4}$	$^c \approx 10^{-5}$
k	J/(s.m.K)	Thermal conductivity	0.59	^{b}30	$^c \approx 30$
C_p	J/(kg.K)	Specific heat	4180	^{a}381.5	$^c \approx 800$
κ	m^2/s	Thermal diffusivity	$1.4\ 10^{-7}$	$1.3\ 10^{-5}$	$\approx 4\ 10^{-6}$
σ	1/(Ωm)	Electrical conductivity	–	$^a 3.87\ 10^6$	$^c \approx 10^6$
λ	m^2/s	Magnetic diffusivity	–	0.21	≈ 1
r_e	m	Outer Radius	0.11	0.11	$3.48\ 10^6$
r_i	m	Inner Radius	0.04	0.04	$1.22\ 10^6$
D	m	Shell gap	0.07	0.07	$2.26\ 10^6$
Ω	rad/s	Rotation rate	$20 - 80$	$40 - 80$	$7.29\ 10^{-5}$
g_D	m/s^2	Gravity at radius D	$30 - 480$	$90 - 480$	7
ΔT	K	Temperature difference	$0 - 25$	$0 - 30$	?

Table 1: Physical parameters and geometric constants of the experiment. ^{a}: Sabot and Lauvray (1995); ^{b}: Okada and Ozoe (1992); ^{c}: estimated from properties of liquid iron at melting point given in Stacey (1992).

1 Introduction

It is widely believed that the self-sustained dynamo of the Earth draws its energy from thermal (and solutal) convection in its liquid metallic outer core. The dynamo mechanism requires that the advection of the magnetic field by the convective flow be much larger than its diffusion. This means that the magnetic Reynolds number $Re_m = UD/\lambda$ (where U is a typical velocity, D the thickness of the liquid core, and λ the magnetic diffusivity, see table 1) has to be larger than about 100. In liquid metals, the ratio of magnetic diffusivity over kinematic viscosity ν is of the order of 10^6, so that the usual Reynolds number $Re = UD/\nu$ is expected to be of the order of 10^8. The convective flow responsible for the dynamo is therefore probably in a very turbulent state. However, it is also very much constrained by the influence of rotation, since the Coriolis force is one of the dominant forces in the system. This has given birth to several fundamental investigations of the properties of convection in a rapidly rotating sphere.

This type of convection is characterized by a small Ekman number $E = \nu/\Omega D^2$, where Ω is the rate of rotation of the Earth, see table 2. The Rayleigh number Ra measures the vigor of convection. The dominence of rotation yields two major effects: convective cells take the shape of vortex columns aligned with the axis of rotation as a consequence of the Taylor-Proudman constraint, and the onset of the convective instability occurs for a larger Rayleigh number than in the non-rotating case, demonstrating the stabilizing effect of rotation in this configuration. These results were first established from the theoretical analysis of the onset of convection in a rapidly rotating spherical fluid shell (Roberts, 1968; Busse, 1970). In the asymptotic limit $E \to 0$, these studies also showed that the width of the columns scales as $E^{1/3}$, with dissipation occuring in the bulk of the liquid, and the critical Rayleigh number Ra_c increases as $E^{-4/3}$. The analysis of Busse for an annulus with tilted upper and lower boundaries highlighted the role of the tilt in controling both the above scalings and the azimuthal structure of the cells: as liquid columns migrate from the inner boundary of the model towards the outer boundary, they have to contract in the direction of

Number	Name	Exp. water	Exp. gallium	Earth's core
$Ra = \frac{\alpha \Delta T g_D D^3}{\kappa \nu}$	Rayleigh number	$3Ra_c - 80Ra_c$	$Ra_c - 10Ra_c$	?
$E = \frac{\nu}{\Omega D^2}$	Ekman number	$10^{-5} - 10^{-6}$	$10^{-6} - 10^{-7}$	$10^{-15} - 10^{-13}$
$P = \frac{\nu}{\kappa}$	Prandtl number	7	$0.022 - 0.027$	$0.1 - 1$

Table 2: Dimensionless parameters for the study of thermal convection. Ra_c is the critical Rayleigh number.

the rotation axis and elongate in the perpendicular directions. Contracting columns acquire a negative vorticity, while columns moving inwards acquire positive vorticity. This is the basic mechanism at the origin of Rossby waves, which propagate in the prograde azimuthal direction. At the onset of convection, the convective columns are thus inclined in the prograde direction, by an angle that depends on the curvature of the boundaries.

These theoretical findings have been largely confirmed by the pionnering experimental studies of Busse and co-workers (Busse and Carrigan, 1976a,b; Carrigan and Busse, 1983; Chamberlain and Carrigan, 1986), and also by the numerical analysis of the onset of convection in spherical shells (Zhang, 1992). However, it became clear that discrepancies existed between the numerical results and the predictions of the local theory of Busse, especially when comparing the critical Rayleigh number for liquids with a small Prandtl number (Zhang, 1992). This has to do with the fact that the preferred lateral dimension of the columns (of order $E^{1/3}$) is small with respect to the shell thickness. It is only recently, that Jones et al. (2000) could solve the problem and propose a fully consistent asymptotic approach.

The understanding of marginal stability analyses allows to explore the field of finite amplitude convection, which has been investigated both in numerical simulations (Sun et al., 1993; Cardin and Olson, 1994; Ardes et al., 1997; Tilgner and Busse, 1997; Grote et al., 2000) and in laboratory experiments (Cardin and Olson, 1992; Cordero, 1993; Sumita and Olson, 2000). Recent numerical models describe a variety of boundary conditions, and achieve Prandtl numbers of order 1, fairly low Ekman numbers ($E = 10^{-5}$), and Rayleigh numbers up to 50 times critical. Experiments are usually done with water ($P = 7$), for Ekman numbers down to 10^{-6} and Rayleigh numbers up to 100 times critical. In all cases, the main characteristics presented above are retained: columnar vortices aligned with the axis of rotation, of small lateral extent, form near the inner sphere and travel around it. However, nonlinear convection also exhibits a number of distinct features that were revealed by these studies: Rossby waves turn into quasi-periodic plumes originating at the inner boundary, still tilted in the prograde direction. The pattern still drifts, but this is not the consequence of wave propagation anymore, but of a real zonal circulation that can be strong when compared to convective velocity. A transition to chaotic (in the sense of unpredictable, highly time dependent, statistically stationary) regimes has been found for Ra/Ra_c as low as 10 when using fluids with a Prandtl number around 1.

In an effort to mimic the effect of very small Ekman numbers, Grote et al. (2000) examined the case of a stress-free outer sphere. Very large zonal velocities were observed, which yield to intermittency as the zonal flow tends to wipe out the convective structures from which it draws its strength. It would be interesting to see if this be-

havior is really characteristic of low Ekman number convection even when dissipation occurs in the boundary layers rather than in the interior of the fluid. This appears to be a difficult challenge for numerical modeling, since it is generally accepted that the computer power needed to resolve nonlinear effects such as turbulence grows with the cube of the highest frequency to resolve, but in the rotating case it is even worse, because of the existence of active thin boundary layers (thickness $O(E^{1/2})$). Approximations have been worked out to extend the parameter range, among which the use of hyperdiffusivities (Glatzmaier and Roberts, 1995), and a quasigeostrophic model to make the problem two-dimensional (Cardin and Olson, 1994). This latter approach is particularly promising, but, as we shall see later, care must be taken to model the friction in the boundary layer located near the outer boundary of the model in an appropriate way.

The lowest Ekman numbers have been reached in laboratory experiments. For fully developped convection, vortices are found to occupy a large part of the spherical shell. Convective plumes originate from both the inner and the outer boundaries. Sumita and Olson (2000) observed a sizeable retrograde zonal velocity, and showed, in the continuation of the work by Cardin and Olson (1994), that it could be explained with a simple model of Reynolds stresses, implying that inertial effects were present.

In any case, the extrapolation of the results available so far to core conditions requires sound scaling relationships. Only a few studies have addressed this question (Cardin and Olson, 1994; Zhang and Gubbins, 2000; Jones, 2000). To be reliable, these relationships have to be derived in the proper regime. However, it appears that the Reynolds number in these studies is never larger than about 100, meaning that viscosity remains an important ingredient in the interior of the shell, in contrast to what is expected in the core. This problem is the main motivation for our study. We have performed laboratory convection experiments in a rapidly rotating sphere. In contrast to previous studies, which focused on the characterization of the convective structures using optical visualization methods and local temperature records, we obtain quantitative velocity measurements using a Doppler ultrasonic technique. Both radial and zonal velocity profiles have been measured, and we have determined how the retrieved characteristic velocities scale with the controlling parameters E and Ra. However, the main originality of our study is the use of two different working liquids: water ($P = 7$) and gallium ($P = 0.027$). Larger inertial effects are expected for gallium because of its low Prandtl number. Indeed, the measured radial velocities u_r indicate that the maximum Reynolds number attained is of the order of 250 for water and 2000 for gallium. A striking observation is that zonal velocities are much larger in gallium than in water. Indeed, the ratio u_θ/u_r, where u_θ is the zonal velocity, can exceed 2 in the gallium experiments whereas it remains lower than 0.7 in the water experiments. These two observations suggest that an inertial regime has been reached in gallium. We derive scaling relationships for this regime and show that they fit our measurements. In particular, we show that the large zonal velocities measured for gallium result from a balance between Reynolds stresses in the interior of the shell and viscous stresses in the Ekman layers of the outer boundary.

We believe that the scaling relationships we obtain permit a better extrapolation to core conditions. Of course, the presence of a magnetic field in the core is likely to affect the force balance to a considerable extent (Chandrasekhar, 1961; Brito et al., 1995; Aurnou and Olson, 2001), but we think that our results without a magnetic field are an important step towards a better understanding of the geodynamo.

In the next section we describe the experimental set-up. In section 3 we determine numerically the critical values and discuss the bidimensionality of the flow. In section 4 we present the velocity profiles for water and gallium, discuss their properties and show how we extract a set of scalar data to be used in the scaling analysis. The evolution of these data as a function of the control parmeters E, Ra/Ra_c and P is exposed in section 5. In section 6 we propose a scaling model, which is found to provide a good fit to the data. We discuss the implications of our results in section 7 and propose an extrapolation to the core.

2 Experimental set-up

The set-up (figure 1, and table 1) is a traditional centrifugal gravity experimental device, as pionneered by Busse and Carrigan (1976b): a sphere of radius 110 mm, filled with either water or gallium, can be spun up to speeds of order 1000 rpm by a 1.4 kW brushless motor, with a stability better than 0.1%. The sphere is transversed by a cylinder of radius 40 mm, coaxial with the rotation axis. The aspect ratio between boundaries is therefore 0.36.

The inner cylinder is made of copper, with the outer 3 mm replaced by polyethylene everywhere except for the 110 mm-high central part, in order to simulate a "central" heat flux. Two distinct spheres have been built: a lexan sphere for use with water, and a copper sphere for use with gallium. This choice has been guided by several requirements: one is to perform optical visualisations in water (see figure 3), one other is to use an excellent heat conductor with gallium, and the third is to obtain a good transmission of ultrasonic waves, taking care of the acoustic impedance adaptation.

The inner temperature (T_1) is fixed by circulating cold water in six channels within the inner cylinder. The cooling power of the device is 1 kW. Two rotary joint units allow the cold water to flow from the Earth-bound frame into the rotating frame. The whole device is installed in a thermostatic chamber, whose function is to set the hot external temperature (T_2). With gallium we had to complete the set-up with a 4 kW electric heater wired around the copper sphere. The heat transfer from the surface of the sphere is indeed not large enough to absorb the large quantity of heat conducted or advected in the liquid metal. The thermostatic chamber then helps maintaining gallium above its solidification point (29.8^oC).

The imposed temperature gradient is opposite to that of the Earth's core because the centrifugal gravity is opposite to the radial gravity of a self-gravitating body. Doing so, one obtains destabilizing buoyancy forces. The difference between the cylindrical symmetry of gravity in the experiment versus spherical symmetry for the Earth has little importance, since in the asymptotic quasigeostrophic state, only the component of gravity perpendicular to the rotation axis plays a dynamic role, the other component being balanced by a pressure gradient (Busse and Carrigan, 1976b; Glatzmaier and Olson, 1993).

Electric signals are passed through slip rings. A set of 10 analogic amplifiers is mounted in the rotating frame, to allow weak signals from thermocouples to be amplified before passing through the slip rings. Filling and emptying operations of the fluid shell are done under argon atmosphere when using gallium, to prevent

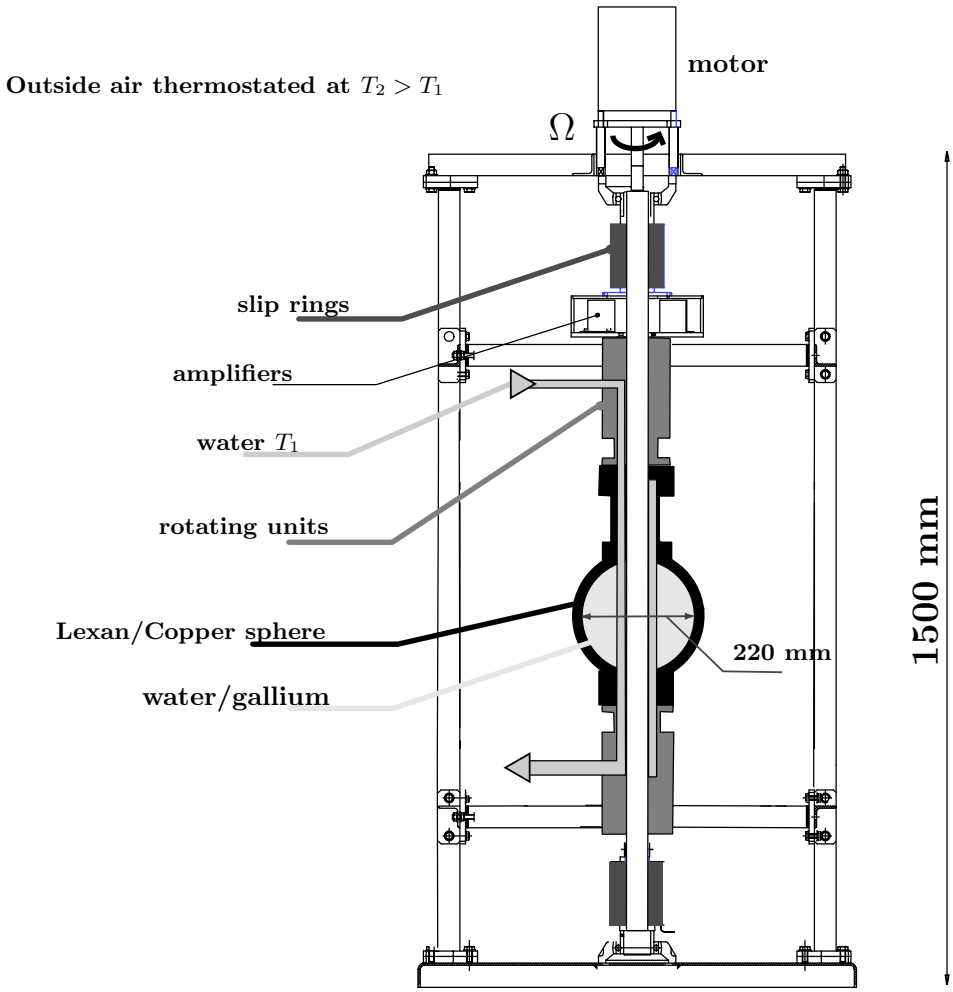

Figure 1: Sketch of the convection device.

oxydation.

The device has been instrumented for thermal measurements: two platinum thermoresistive probes record the temperatures of the inner cylinder and outer sphere. Typical temperature variations at these boundaries are found to be less than 0.2 K during a run. Thermocouples (Iron/Constantan in water, and Platinum/Constantan in gallium, the liquid metal providing electrical contact) record temperature fluctuations (less than 2 K) at the surface of the inner cylinder, 25 mm above and below the equator.

The originality of our experiment is the implementation of ultrasonic pulsed Doppler velocimetry. This technique relies on echoes backscattered by small inhomogeneities of the fluid. From the time delay and Doppler shift of echoes can be retrieved the reflector's position and component of velocity along the ultrasonic beam. One thus obtains profiles of flow velocity (Takeda, 1986). Brito et al. (2001) validated the technique for use with water and gallium, measuring zonal velocities in a prescribed vortex flow. We use the DOP 1000 velocimeter of Signal Processing with 4 MHz cylindrical ultrasonic transducers (TR30405) of length 8 mm and diameter 8 mm. The main challenge is to measure convective velocities (of a few millimeters per second) in a sphere that is rotating at several hundreds of revolutions per minute. This is achieved by mounting the transducers in the rotating frame: they are embedded into the outer sphere in one-end machined holes, at equatorial position, and the electric signal is passed through the slip-rings. This set-up gave excellent results, the main limitation being the contamination of the signals with motor-related electric noise as they pass through the slip-rings.

The top view of figure 2 displays the possible locations of the transducers. The radial beam allows us to retrieve the radial velocity field as a function of radius and time. The lateral beam enters the sphere at a normal angle of 40^o and is refracted to normal angles of 24.5^o and 21.5^o respectively by the lexan/water and copper/gallium interface. The closest approach of the beam to the inner cylinder is 5 mm in water and 1 mm in gallium. This profile contains a combination of radial and zonal velocities, from which the latter can be extracted (see appendix for exact values of angles and procedure for the retrieval of mean zonal flow).

Another difficulty is the seeding of the liquids in order to obtain sufficient echoes. Neutral buoyancy is crucial, because of the large centrifugal forces present in the rotating frame. In water, the best results were obtained with pine pollen particles of typical dry size 20 μm. These particles fill with water and become neutrally buoyant (B. Andreotti, personal communication, 2000). In gallium we used Zirconium Boride with density 6.17, close to that of gallium, and a size of order 50 μm. It is also likely that gallium oxide particles act as inhomogeneities. In the gallium experiments, boundaries such as the copper part of the inner cylinder and the copper sphere were coated with a thin cataphoretic film, in order to ensure wet contact with gallium, and easy removal of oxides that scatter the ultrasonic beam (Brito et al., 2001).

Note that the use of ultrasonic Doppler velocimetry was dictated by the need to measure velocities in opaque liquid gallium. However, even in transparent water where visualization is possible, the quantitative information it provides is valuable for the determination of scaling laws as presented in this article. By using a set of several neighbouring multiplexed transducers, it is also possible to investigate the local velocity structure of the convective flow.

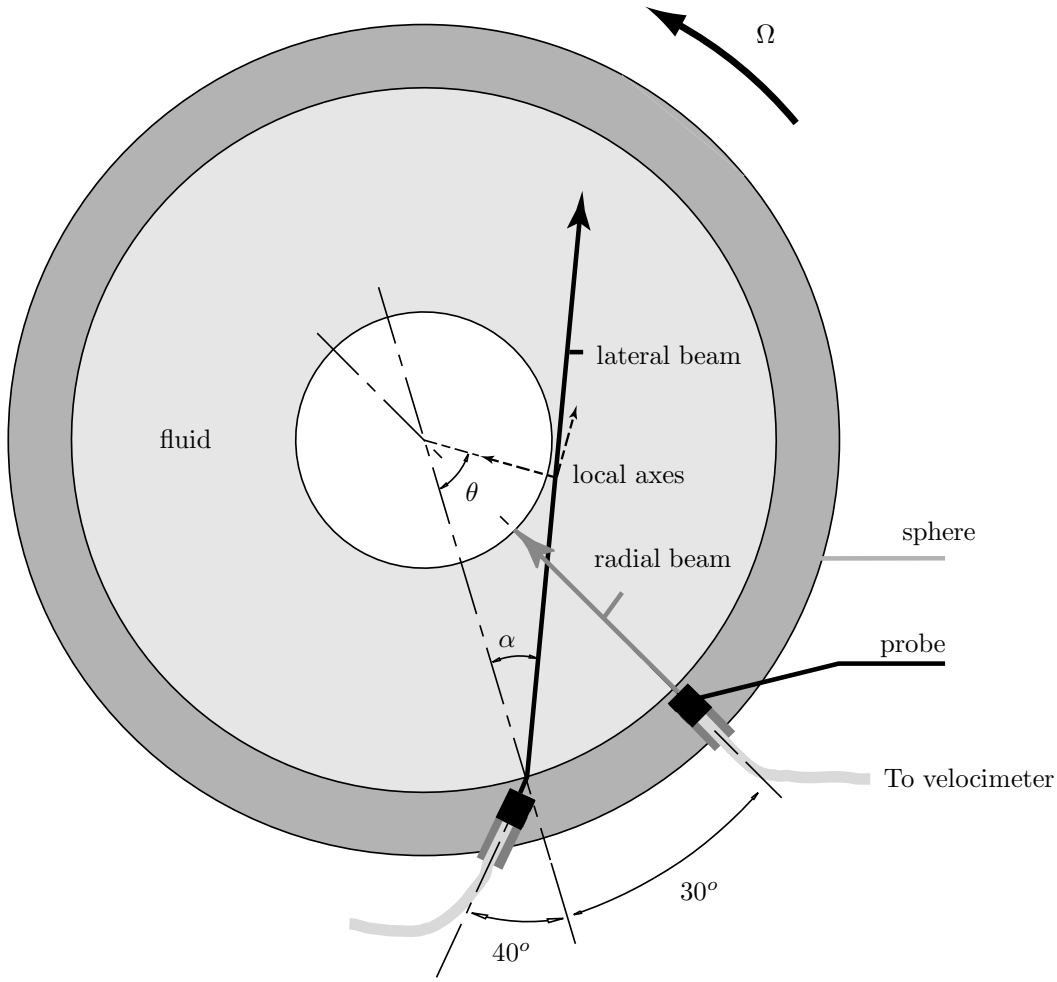

Figure 2: Top view of the equatorial plane, with locations of transducers.

P	E	Ω (rpm)	Ra_c	ΔT (K)	ω_c	τ_c (s)	m_c
7	$9.7\ 10^{-6}$	200	$9.6\ 10^6$	0.65	$1.3\ 10^2$	246	17
7	$4.8\ 10^{-6}$	400	$2.3\ 10^7$	0.39	$2.1\ 10^2$	145	22
7*	$3.3\ 10^{-6}$	600	$4\ 10^7$	0.30	$4.3\ 10^2$	114.2	25
7*	$2.4\ 10^{-6}$	800	$5.8\ 10^7$	0.25	$5.2\ 10^2$	92.3	28
0.027	$1.5\ 10^{-6}$	400	$1.2\ 10^7$	8.5	$1.2\ 10^4$	8.6	15
0.027	$9.7\ 10^{-7}$	600	$1.9\ 10^7$	6.0	$1.7\ 10^4$	6.3	17
0.027	$7.3\ 10^{-7}$	800	$2.7\ 10^7$	4.8	$2.0\ 10^4$	5.2	19

Table 3: Critical values from numerical simulations. Stars denote extrapolated data.

3 Basic properties of the flow.

In this section, we discuss properties of the flow which are needed for the forthcoming analysis. This includes a determination of the threshold of convection, a check of the two-dimensional character of the flow, with an assessment of the role of thermal wind.

3.1 Onset of convection

Our experimental set-up was built to study fully developed convection. It is not well suited for the investigation of the onset of convection. In order to scale our measurements, we need to determine the critical Rayleigh number. Therefore numerical marginal stability simulations have been performed, with a 3D code from Dormy et al. (1998), validated through the Dynamo Benchmark initiative currently in progress (Christensen et al., 2001). We have solved the eigenvalue problem by iteration of the linear part of the code. The model contains a spherical inner core with 0.35 aspect ratio, no-slip and fixed temperature boundary conditions, radial gravity. Solutions have been computed for two values of the Prandtl number : 7 (water) and 0.027 (liquid gallium). Ekman numbers as low as $4.9\ 10^{-6}$ and $4.9\ 10^{-7}$ have been reached respectively for $P = 7$ and $P = 0.027$. In order to reach the experimental Ekman number values, some extrapolation has been done for $P = 7$, using the asymptotic laws.

Table 3 summarizes the numerical results. Ω is the dimensional rotation rate, ΔT the dimensional temperature difference, m_c is the critical azimuthal wavenumber, ω_c is the non-dimensional critical pulsation of the Rossby wave (the time scale is D^2/ν), and τ_c its dimensional period. Note that all the numerical experiments predict that flow is two-dimensional indeed in these low-Ekman number situations. At $E = 9.7\ 10^{-6}$ in water we have experimentally bracketed the critical temperature difference using temperature signals on thermocouple probes: $0.8\ \mathrm{K} < \Delta T_c < 1.2\ \mathrm{K}$, which is somewhat higher than the numerical value. The discrepancy probably has to do with the difference in geometry of the inner boundary, and to the presence of thermal wind, unless the sensitivity of the method is not good enough to access the threshold of convection. Critical values used in this manuscript are always those derived from the numerical simulations.

3.2 Vertical structure of the flow

All numerical simulations of the convection onset have shown that because of the Proudman-Taylor constraint, which governs the low-Ekman number situation we consider, the convective vortices are columns aligned with the axis of rotation. However, z-invariance may be destroyed by the increasing buoyancy forces at higher Ra/Ra_c, and by thermal wind, which is not present in the numerical simulations, but plays a role in the experiment, due to the fact that the gravity equipotentials are not parallel to the isothermal surfaces (Busse, 1970).

Vertical invariance of the flow has been checked optically in all experiments performed in water, as illustrated by the photograph of figure 3. Vertical white lines are due to the alignment of Kalliroscope flakes oriented by the convective columns. In gallium, this type of direct visualization is not possible. We therefore rely on the temperature measurements displayed in figure 3. The 200 seconds-long records are from two thermocouples located at the surface of the inner cylinder, 25 mm above and below the equator in the vertical z direction. The two signals are strongly correlated over a very long timescale, indicating that temperature is advected by a velocity field with low vertical shear. Temperature measurements in water yield the same behaviour. Therefore, we are confident that all the velocity profiles measured in the equatorial plane by ultrasonic Doppler velocimetry are representative of the full velocity field, apart from boundary layers.

Next we turn to thermal wind. The zonal velocity induced by thermal wind $\mathbf{u}_{\rm th}$ is governed by the following equation (Busse, 1970):

$$2(\mathbf{\Omega}\cdot\nabla)\mathbf{u}_{\rm th} = \alpha\nabla T \times \mathbf{g}_{\rm cen}$$

where $\mathbf{g}_{\rm cen} = \Omega^2 r$ is the centrifugal gravity field. Integrating along a vertical line at constant r yields, for the equatorial value of thermal wind:

$$\mathbf{u}_{\rm th} = -\frac{\alpha\Delta T_r \Omega r}{2}\mathbf{e}_{\boldsymbol{\theta}}$$

where $\mathbf{e}_{\boldsymbol{\theta}}$ is the zonal unit vector and ΔT_r is the temperature difference between the spherical external boundary and the equator at radius r, apart from viscous boundary layers. Thermal wind is retrograde if the outer sphere is hotter than the inner cylinder, i.e. in the case of an adverse (destabilizing, convective) temperature gradient. An estimate in water using $\alpha = 2\ 10^{-4}$ K^{-1} (table 2), $\Delta T_r = 15$ K, $\Omega = 400$ rpm, and $r = 5$ cm yields a value of $u_{th} = 3.2$ mm/s. With a 15 K adverse temperature difference imposed between the boundaries, we have measured zonal velocities using the lateral Doppler probe and found a retrograde flow of only 1 mm/s at $r = 5$ cm. Moreover, thermal wind should induce vertical shear of convection columns, and this has not been observed.

Another estimate in gallium using $\alpha = 1.26\ 10^{-4}$ K^{-1}, $\Delta T_r = 15$ K, $\Omega = 400$ rpm, and $r = 5$ cm yields a value of $u_{th} = 2$ mm/s. Thermal wind should be smaller indeed in gallium, due to a smaller thermal expansion coefficient. With an adverse temperature gradient of 15 K, we have measured a retrograde flow of 2.7 mm/s at $r = 5$ cm, which is, in contrast, higher than the water value. To estimate the thermal wind part of this flow, we have performed the same experiment, with a reverse (stable) temperature gradient of 15 K, and therefore no convection. This yields a prograde flow of only 1 mm/s.

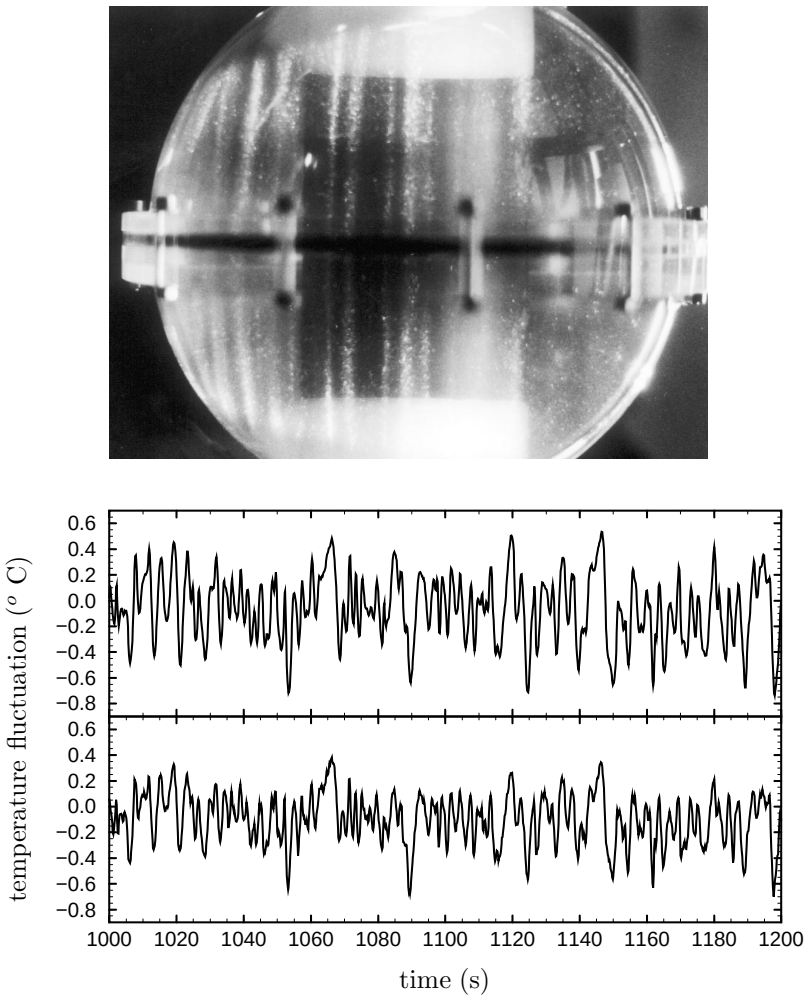

Figure 3: Up: Shear structures visualized in water using Kalliroscope flakes, in a plane containing the rotation axis, close to the inner cylinder. Ekman number is $E = 9.7\ 10^{-6}$, Rayleigh number is 4.2 times critical. Down: vertical correlations between two thermocouple probes located 5 cm away on the inner cylinder, done in gallium. Ekman number is $E = 7.3\ 10^{-7}$, Rayleigh number is 5.0 times critical.

In our set-up, thermal wind tends to be smaller than theoretical estimates using the full temperature difference. We therefore conclude that isothermal surfaces are more cylindrical than expected. This can be explained by the presence of the inner cylinder. Note that convection, when present, also tends to give a cylindrical shape to isothermal surfaces. Moreover, in the gallium case, thermal wind in the reverse situation is only one third of zonal circulation in the adverse situation. From this we conclude that thermal wind is not the predominant driving mechanism for the zonal circulations we observe.

4 Velocity profiles

Results reported in this section summarize the velocity measurements obtained in sequence experiments made at various Ekman and Rayleigh numbers, in both water and gallium. Ekman numbers we have reached in water are $E = 9.7\ 10^{-6}$ (motor speed of 200 rpm) down to $E = 2.4\ 10^{-6}$ (800 rpm), and in liquid gallium they are $E = 1.5\ 10^{-6}$ (motor speed of 400 rpm) down to $E = 7.3\ 10^{-7}$ (800 rpm).

Experimental radial velocity functions have been mapped in a time-depth color-contoured representation (see figure 4.). X-axis is time in seconds, Y-axis is distance in millimeters (the sphere is at $Y = 0$ mm and the inner cylinder at $Y = 70$ mm). Velocity is expressed in millimeters per second. Color red stands for a velocity flowing away from the probe, i.e towards the inner cylinder. The transducer sees a radial velocity function changing with time, assumed to be associated with vortices in the equatorial plane, drifting across the beamline under the influence of either wave propagation or zonal flow as shown in the sketch in figure 5. For a stationary or periodic flow, the time axis could therefore be seen as a (deformed) lateral angle axis. Ultrasonic Doppler velocimetry is not perfect near boundaries. Boundary layers are not resolved, and multiple echoes due to an acoustic impedance contrast between sphere and fluid saturate part of the signal, which is lost near the sphere. This is especially true with the gallium experiment in figure 4.4 where the first 25 mm of the profile is lost.

Figure 4.1 shows a pattern obtained for $Ra = 4.2\ Ra_c$ in water. The experiment corresponds to the photography of figure 3. The velocity amplitude is very small (< 1 mm/s) and it is difficult to extract the velocity signal from noise for lower Ra number. Convection tends to be stronger in the vicinity of the inner cylinder. At any depth, we can appreciate a time oscillation between positive and negative velocity associated with the presence of thermal vortices. Its typical period (between 150 and 200 s) is close to 246 s, the period predicted for the Rossby wave at the onset of convection (see table 3). Moreover, we observe tilted bands approaching the inner cylinder when time goes on. This tilt could be explained by the prograde propagation of vortices spiralled in the prograde direction. For experiment 4.1, in contrast, a low retrograde mean zonal flow of 0.1 mm/s has been measured using the lateral Doppler probe. These observations suggest that the Doppler diagram 4.1. should be interpreted mostly in terms of the propagation of a Rossby wave. The departure from criticality induces loss of periodicity in the wave (vacillating, superposition).

In figure 4.2, Ra is higher up to 22.2 times critical while the Ekman number has been kept constant. The pattern exhibits several significant changes. Periodicity is

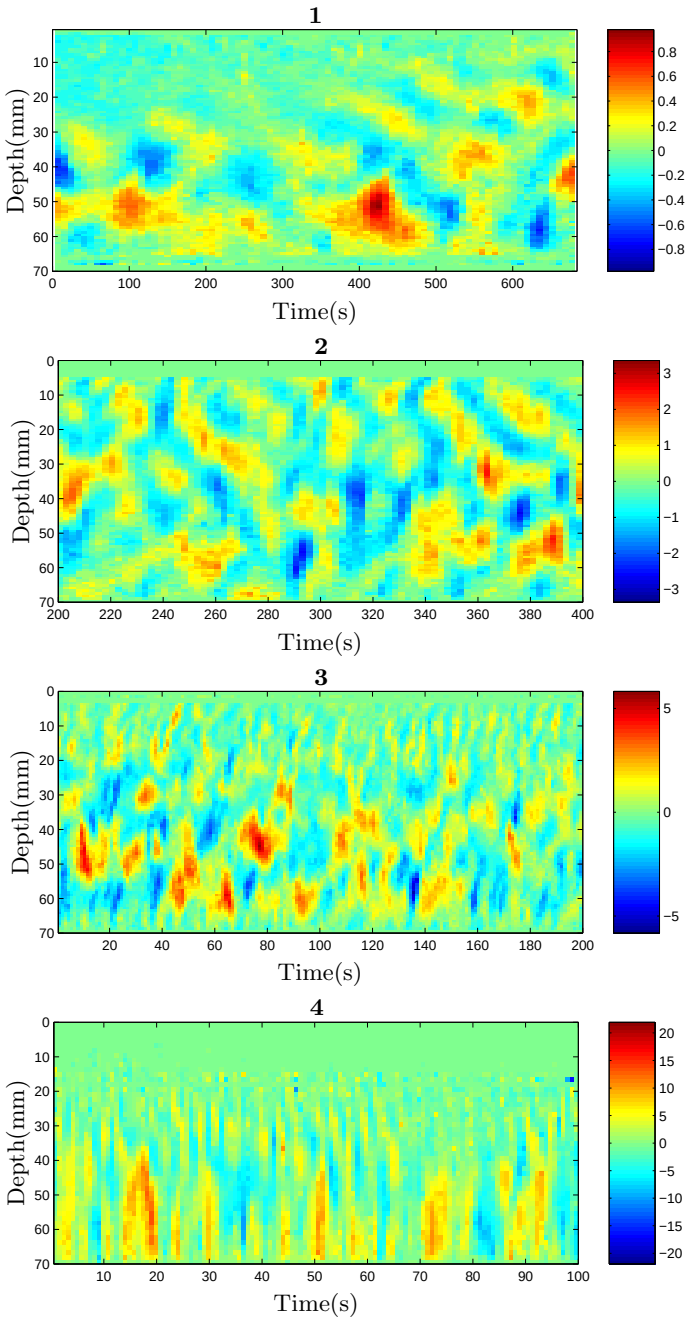

Figure 4: Time-depth radial velocity patterns. Velocities are expressed in millimeters per second. **1**: performed in water, with $Ra/Ra_c = 4.2, E = 9.7\ 10^{-6}$; **2**: performed in water, with $Ra/Ra_c = 22.2, E = 9.7\ 10^{-6}$; **3**: performed in water, with $Ra/Ra_c = 26.6, E = 4.8\ 10^{-6}$; **4**: performed in liquid gallium, with $Ra/Ra_c = 3.2, E = 1.5\ 10^{-6}$.

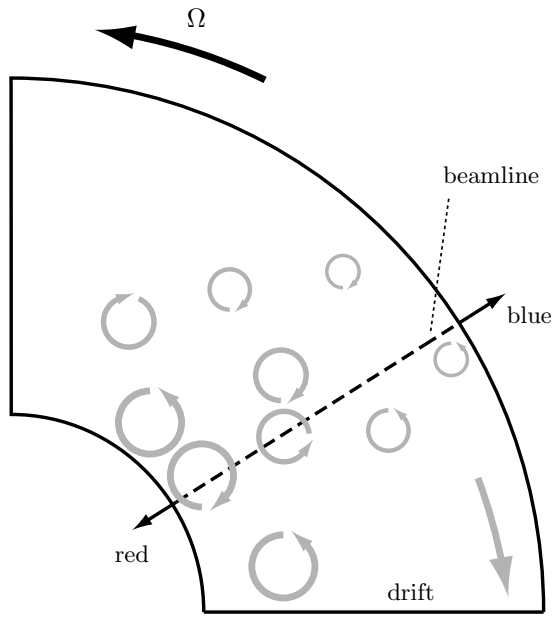

Figure 5: Explanation sketch for time-depth velocity maps.

now completely lost, characterictic time scales are shorter (< 50 s), tilts are different, typical velocities are larger, the distribution of radial sizes has broadened. We have clearly left the pseudo-periodic state of thermal Rossby waves to jump into a fully developed state of convection. In this case, a stronger retrograde zonal flow of 0.5 mm/s has been measured, using the lateral Doppler probe. The importance of zonal advection has therefore grown from case 4.1 to case 4.2. On figure 4.3, the Ekman number is lowered while Ra/Ra_c remains comparable. The state of convection remains the same, but velocities, sizes and durations have changed. The evolution of these characteristics with controlling parameters is discussed in next section.

Pattern 4.4 presents an experiment performed in liquid gallium, Ra/Ra_c is 3.2, a value which is similar to the conditions of pattern 4.1, and Ekman number is $1.5\ 10^{-6}$. Vortices attached to the inner cylinder have grown in radial size. Bands are less tilted, and this suggests that the convective structures are more radial. In that case, the zonal flow (5 mm/s) is very large and we cannot neglect its influence on the time analysis. The lateral size of the columns is presumably larger than in the water case. Anyhow, the gallium experiments never show quasiperiodic flow like in water (pattern 4.1) even for the lowest ratio Ra/Ra_c. We infer this is the main effect of the change when lowering the Prandtl number; the large amplitude of the velocities lead the system to turbulence just above the onset of convection.

The local organization of developed convective flow seems rather intricate on diagrams 4.1–4.4, and we therefore first concentrate on the study of its time averaged mean properties. For the radial velocity field of experiments 4.3 and 4.4, we plot (upper plots of figure 6) the time-averaged standard deviation of velocity $\tilde{u}_r$ against radius (see appendix for definitions of averaging operators used in this study). The error bars account for the reproducibility of measurements, and for uncertainties introduced by the centrifugation of seeding particles.

At a given radius r, we also study the distribution $\delta_r(r)$ defined as:

$$\delta_r(r) = \left((r'_i - r_i), 1 < i < N, \begin{cases} \tilde{u}_r(r'_i, t_i) = 0 \\ \tilde{u}_r(r_i, t_i) = 0 \\ r'_i > r > r_i \\ \forall y \in]r_i, r'_i[, \tilde{u}_r(y, t_i) \neq 0 \end{cases} \right).$$

N is the total number of profiles acquired during a run (see appendix) and t_i the time of profile i. δ_r is therefore the distribution of radial cell sizes around r. At any given depth, the histogram of δ_r is built. Figure 14 of the appendix shows an example of such an histogram. The lower plots of figure 6 represent the mean $\overline{\delta_r}$ of δ_r as a function of r. The error bar is the standard deviation $\tilde{\delta_r}$ of δ_r, and it accounts for the variety of cell sizes present around a given radius.

Figure 6 shows that when convection is developed, the instability extends throughout the space between boundaries, but most of the energy is located near the inner cylinder. The flow slows down, and vortex size decreases, as r increases (see section 6 for an interpretation). Figure 7 is a plot of mean zonal velocity $\overline{u_\theta}$ retrieved using the azimutal probe (see appendix for details). Error bars on $\overline{u_\theta}$ are of the same origin as those on $\tilde{u}_r$. Experimental parameters are close to those of patterns 4.3 and 4.4. The two zonal flows are retrograde near the inner cylinder. In most experiments done with gallium, we could appreciate a weak prograde zonal flow at larger radius. At even larger radius in gallium (broken lines in figures 6 and 7) energy peaks due to the impedance contrast between copper and gallium blind the ultrasonic measurement.

Zonal flow in gallium is comparable to convective flow, whereas in water it is lower. In the latter case, the observed radial variations are most probably due to an incomplete averaging of convective signal, and therefore not significant. The gallium profile clearly shows a maximum velocity close to the inner cylinder, coincident with the maximum of convective velocity, and relaxes to zero on the typical size of convection cells. Nonzero mean zonal flow can be associated to geostrophic motion along cylinders of constant r, and with this interpretation, two scales naturally appear in the flow: the scale of columns (which will be denoted as convective scale), and the scale of the container for geostrophic motion.

5 Evolution with control parameters.

The radial shape of time averaged mean properties, seen in the previous section, is a robust feature of the experiments we have conducted. We can infer that this shape scales homothetically with control parameters in the range covered by experiments. We therefore can separate the study of radial dependence in one hand, and the study of the homothetic scaling of a particular point of the profiles in the other hand. A model for radial dependence will be given in the next section. In this section we concentrate on the scaling of variables picked up at a given radius. We chose the radius r_{max} where the flow is stronger (maximum of $\tilde{u}_r$), to increase the signal to noise ratio.

This way we follow the evolution of $\tilde{u_r}(r_{max})$, $-\overline{u_\theta}(r_{max})$, and $\overline{\delta_r}(r_{max})$, with error bars as defined above, with the controlling parameters E, Ra/Ra_c, P. We also

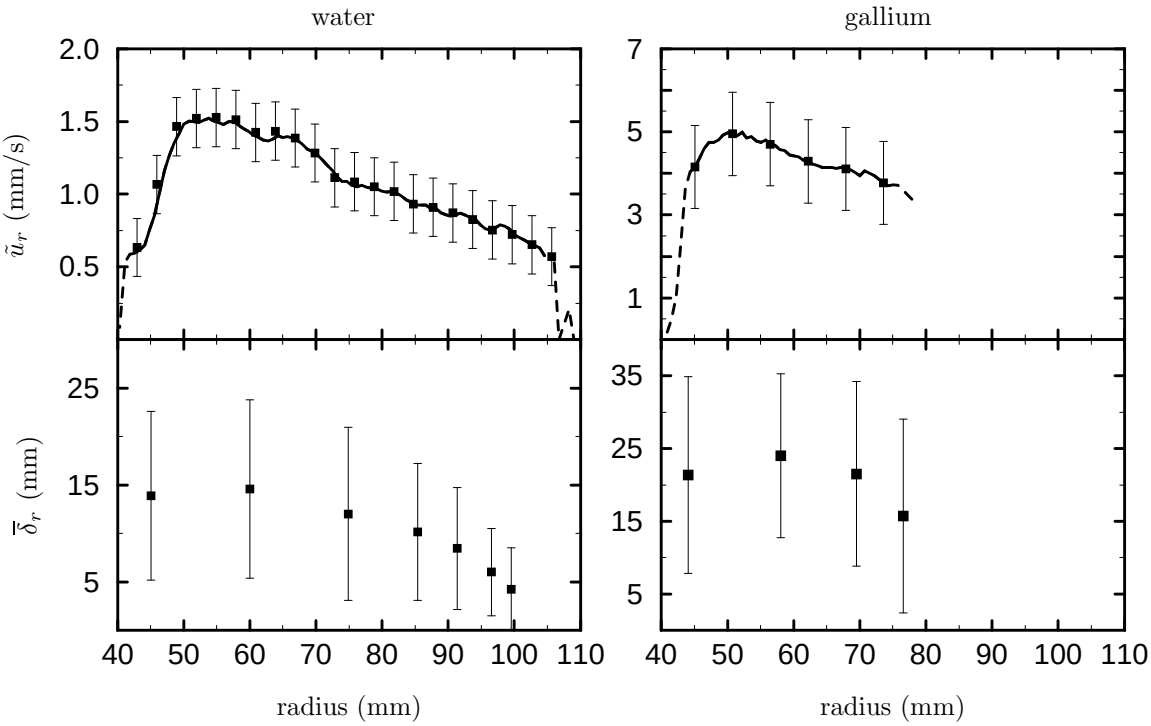

Figure 6: Mean properties for the flow extracted from patterns 3 and 4. Broken line in gallium plots of this figure and figure 7 highlights the region where the signal is saturated by multiple echoes due to the impedance contrast between copper and liquid gallium.

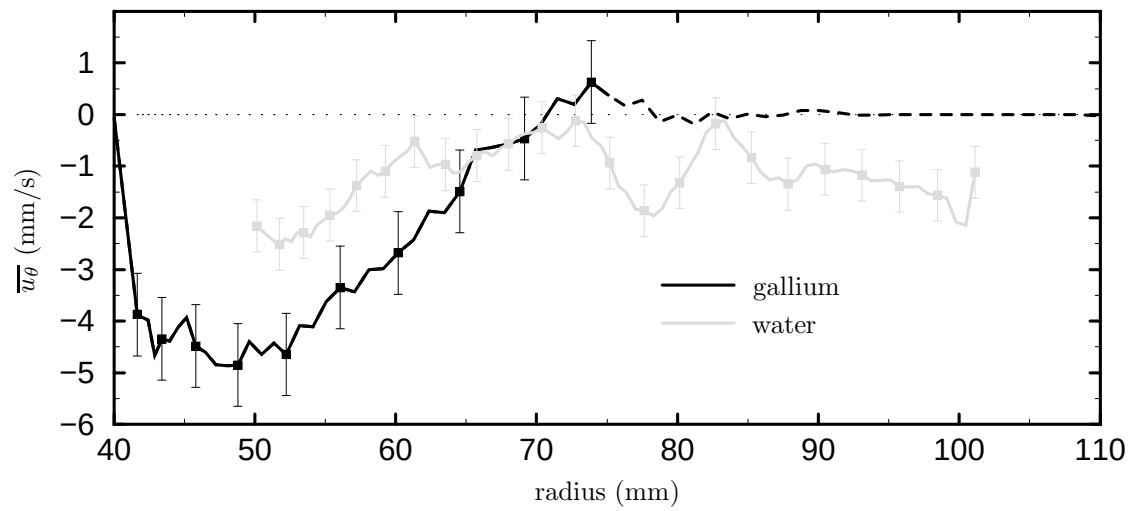

Figure 7: Mean zonal flow $\overline{u_\theta}$ in water (experiment 5: $E = 4.8\ 10^{-6}, Ra = 31 Ra_c$), and gallium (experiment 6: $E = 1.5\ 10^{-6}, Ra = 3.2 Ra_c$).

follow the evolution of the mean time $\overline{\Delta t}(r_{max})$ elapsed between two zeros of the radial velocity function, at the given radius r_{max}, with error bars corresponding to $\tilde{\Delta} t(r_{max})$.

Figure 8 displays the resulting dataset, as a function of the departure from criticality $Ra/Ra_c - 1$. The horizontal error bars incorporate the fluctuations of the temperature gradient during the run. The runs with gallium are for the lower $Ra/Ra_c - 1$, on the left, while those for water have higher $Ra/Ra_c - 1$. The different symbols are for different Ekman numbers. The top two graphs give the evolution of the two components of velocity. For both liquids, velocities increase with the departure from criticality and also increase when the Ekman number is decreased. For a given $Ra/Ra_c - 1$, both $\tilde{u_r}$ and $\overline{u_\theta}$ are clearly much higher in gallium than in water. While it is expected to be zero in a purely viscous regime with no thermal wind, we always measure a retrograde zonal velocity at radius r_{max}. Nonzero retrograde zonal velocities have been observed experimentally (Sumita and Olson, 2000), and numerically (Cardin and Olson, 1994). This last study demonstrated that they could be explained in terms of the Reynolds stresses that result from non-linear inertial effects. Our quantitative measurements of the average zonal velocity confirm this observation and show that this effect is much larger in gallium. Cordero and Busse (1992) also invoked a retrograde zonal flow to explain temperature measurements in water experiments very close to the threshold of convection, in a narrow-gap configuration. They attributed this velocity to thermal wind. We have seen before that it was certainly not the predominant driving mechanism for the large zonal velocities we observe. Moreover, in experiments done in gallium, a weak prograde zonal flow has been observed at large radius. This is not compatible with a thermal wind explanation, since it requires a reverse temperature gradient to produce prograde zonal circulations.

The next two graphs deal with the dimensions of the convective cells. We first examine the variation of the average radial dimension $\overline{\delta_r}$. For water at moderate Rayleigh number, we note that $\overline{\delta_r}$ decreases as the Ekman number decreases. This is the expected behaviour, as size scales with $E^{1/3}$ in the geostrophic viscous regime that prevails at the onset of convection. However, we find that for the lowest Ekman numbers in water, and for experiments in gallium (which provide the largest radial dimensions), the mean of the cell size distribution generally increases with the Rayleigh number. This suggests that the size of the convective cells is no longer controlled by a geostrophic viscous balance, but rather depends on non-linear effects that increase when the Rayleigh number increases.

With our present set-up, we cannot access directly the dimension of the convective cells in the azimuthal direction. However, from the spatio-temporal maps of the preceeding section, we measure the mean time $\overline{\Delta t}$ elapsed between two zeros of the radial velocity function. If a cell of lateral extent $\overline{\delta_\theta}$ drifts across the line of measurement with an azimuthal velocity $\overline{u_\theta}$, it will result in a time signal with $2\overline{\Delta t} = \overline{\delta_\theta}/\overline{u_\theta}$. In water, we observe that $\overline{\Delta t}$ decreases when either E is decreased or Ra increased. For gallium, $\overline{\Delta t}$ is short as a consequence of the large zonal velocity. Later in this article, we will try to single out the variation of $\overline{\delta_\theta}$.

From the previous results, we derive the local convective Reynolds number : $Re_l = \tilde{u_r}\overline{\delta_r}/\nu$. Its variation is plotted in the next graph of figure 9. The data show a regular increase of the local Reynolds number with Ra/Ra_c for both water and gallium. The striking observation is that the Reynolds number is much higher in the gallium experiments, where it reaches 600, than in the water experiments, where 80 is the

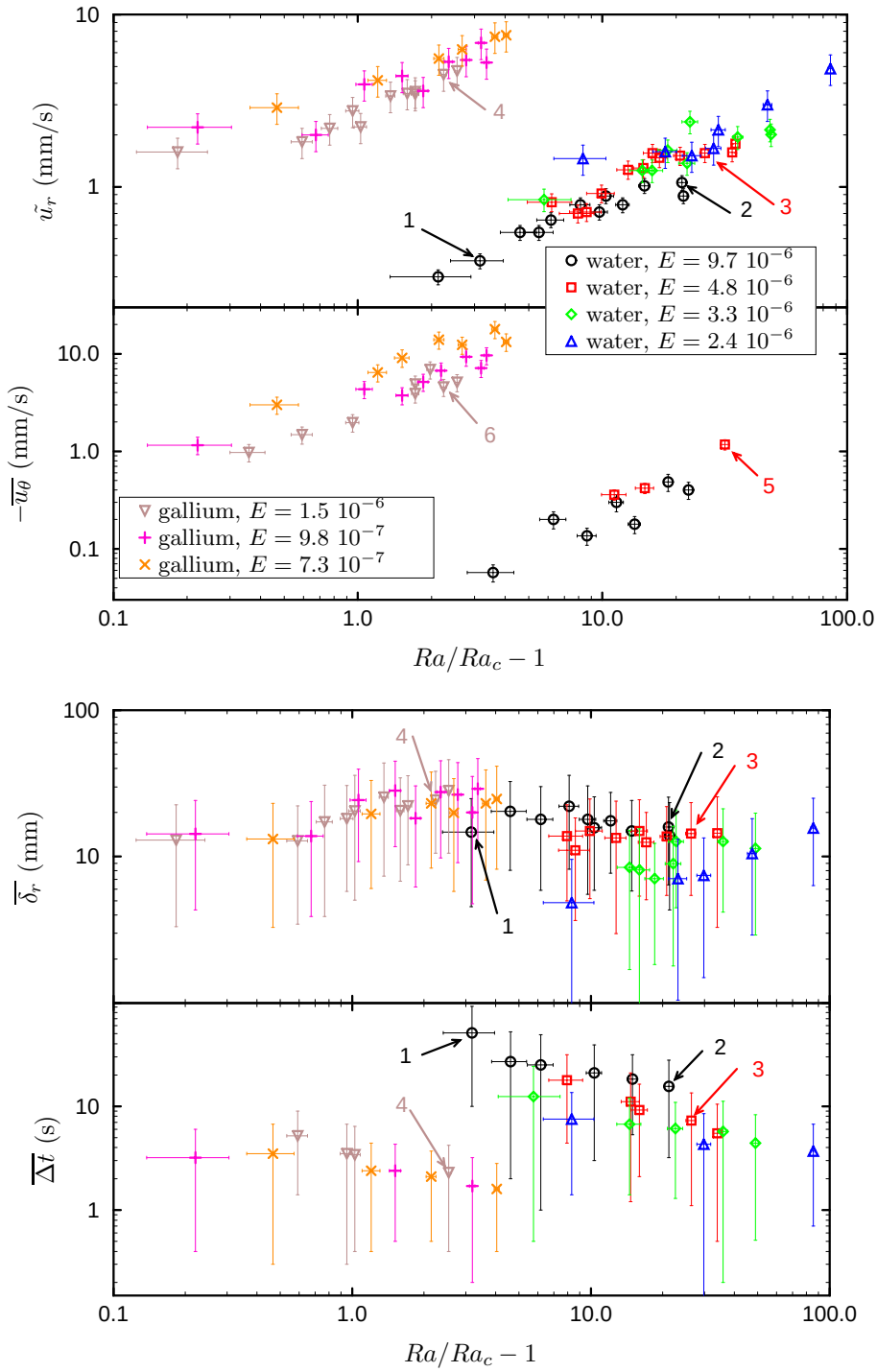

Figure 8: Scalar data extracted for scaling. Arrows 1–4 denote data points corresponding to shown velocity patterns (figure 4). Arrows 5 and 6 correspond to zonal flows shown on figure 7.

largest value, despite the fact that the Rayleigh number is much larger than Ra_c in this case. This is of course due to the larger convective velocities observed in gallium, together with the fact that the kinematic viscosity of gallium is about 3 times smaller than that of water. If we were to use the thickness of the shell rather than $\overline{\delta_r}$ in the definition of the Reynolds number, we would reach values of 2000 for gallium and 250 in water. Therefore, we expect non-linear effects to be fully developped in gallium, while they probably compete with viscous dissipation in water.

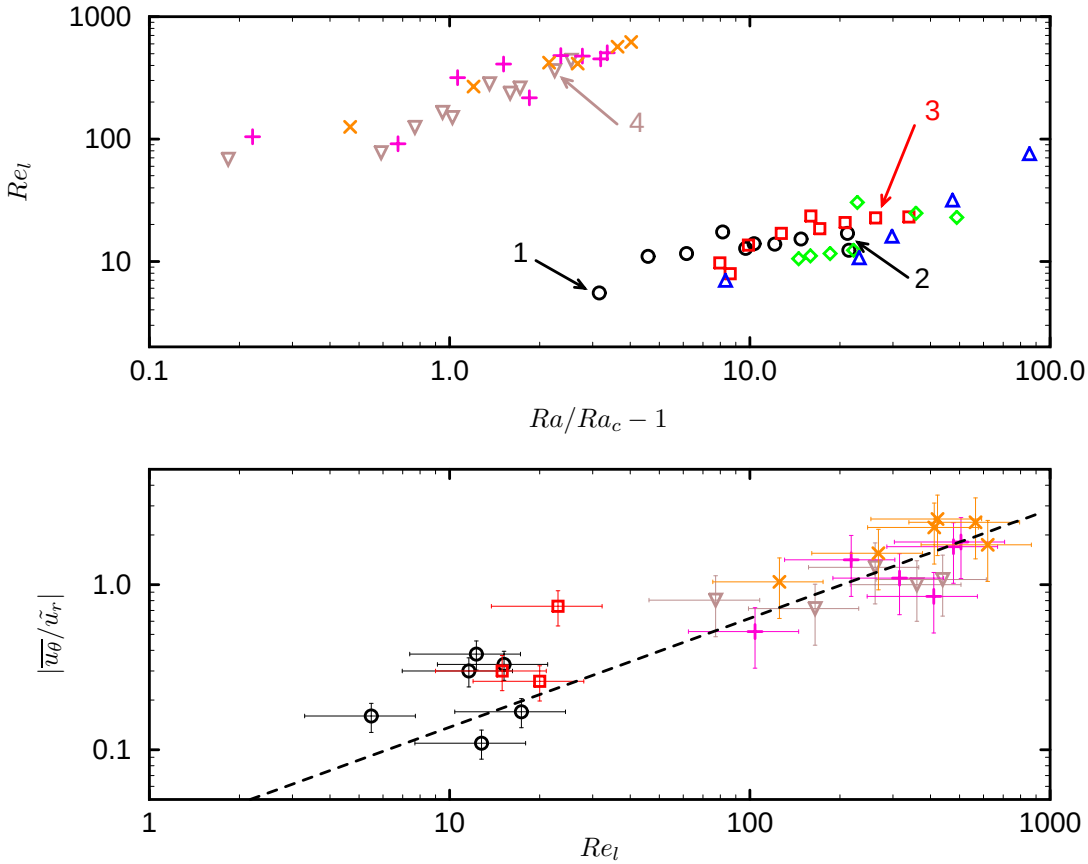

Figure 9: Scalar data (continued).

Since we anticipate that zonal velocities are caused by Reynolds stresses, we expect that they increase as the Reynolds number increases. This is best seen by plotting the ratio $|\overline{u_\theta}/\tilde{u}_r|$, which is a dimensionless quantity, versus Re_l. The results are shown in the last graph of figure 9. While this ratio is less than 0.7 in the water experiments, it reaches 2.5 in the gallium experiments, where the Reynolds number is the largest. The results presented in this section demonstrate the interest of comparing the properties of convection for liquids with different Prandtl numbers. The behaviour observed for gallium, which has a low Prandtl number, with high Reynolds number and large zonal velocities, strongly suggests that convection is dominated first by the Coriolis force and second by non-linear inertial terms. In the next section, we perform a scaling analysis to test this idea.

Number	Definition	Experiment	Earth's core
$Bu = \dfrac{\alpha g \delta T}{\Omega U}$	Busse	< 0.1	$< 10^{-2}$
$Ro = \dfrac{U}{\Omega D}$	Rossby	$< 10^{-2}$	$\approx 10^{-6}$

Table 4: Auxiliary dimensionless parameters justifying the QG approximation in the experiment. δT is the order of magnitude for local temperature perturbations. Estimates are given for the Earth's core, using a typical velocity of 10^{-4} m/s (Jault et al., 1988).

6 Scaling analysis.

In this section, we introduce quasigeostrophic equations and derive scaling relationships for two different regimes: a viscous one and an inertial one. We then compare the predictions of these two approaches to the measurements of the previous section.

The fluid shell is described under the Boussinesq approximation, obeying both Navier-Stokes and heat equations, made dimensionless using D as length scale, D^2/ν as time scale, $P\Delta T$ as temperature scale. A cylindrical frame $\mathbf{e_r}, \mathbf{e_\theta}, \mathbf{e_z}$ is chosen. The momentum and heat equations are:

$$\frac{\partial \mathbf{u}}{\partial t} + (\mathbf{u}\cdot\nabla)\,\mathbf{u} + 2E^{-1}\mathbf{e_z}\times\mathbf{u} = -E^{-1}\nabla\Pi - Ra\; r\mathbf{e_r}T + \nabla^2\mathbf{u}. \tag{1}$$

$$\frac{\partial T}{\partial t} + (\mathbf{u}\cdot\nabla)\,T = P^{-1}\nabla^2 T. \tag{2}$$

Here $\mathbf{u}$ is the fluid velocity, T is the temperature, Π is pressure (including contribution from the gravity potential). Gravity grows linearly with the cylindrical radius r. Equation (1) is subject to no-slip boundary conditions, and equation (2) satisfies imposed temperatures on both the inner cylinder and the outer sphere.

Experimental facts strongly suggest that flow is quasigeostrophic (QG): it is columnar, which means that the order of magnitude of inertia, buoyancy and viscosity are small when compared to Coriolis force (balanced by a pressure gradient). This is confirmed by the quantitative estimates of these ratios, which respectively give the Rossby, Busse and Ekman numbers (see tables 2 and 4). A nonlinear QG model has been derived by Cardin and Olson (1994), from the local marginal stability theory of Busse (1970), under the following assumption: dissipation by friction through the Ekman layers near the outer spherical boundary is neglected. Fields are then expanded into powers of the Ekman number. To leading order a geostrophic balance exists between Coriolis force and the pressure gradient, which implies that flow is two-dimensional at this order. This equilibrium alone cannot solve the problem (geostrophic degeneracy), and to next order the equation governing the column-averaged z-component ω of vorticity is:

$$\frac{\mathrm{d}\omega}{\mathrm{d}t} - E^{-1}\frac{2}{L}\frac{\mathrm{d}L}{\mathrm{d}r}\mathbf{u}\cdot\mathbf{e_r} = \nabla^2\omega + Ra\frac{\partial T}{\partial\theta}, \tag{3}$$

where

$$L = \sqrt{r_e^2 - r^2}$$

is half the height of a fluid column, and dL/dr is thus the local slope of the external boundary. Equation (3) averages the effect of the Coriolis force using the non-penetration condition for velocity at sloping boundaries (Cardin and Olson, 1994). This results in the "vortex-stretching" term

$$\frac{2}{L}\frac{\mathrm{d}L}{\mathrm{d}r}\mathbf{u}\cdot\mathbf{e}_r.$$

This term is found to be larger than Ekman-pumping induced circulation even for fairly low dL/dr. Only in the case of purely zonal velocities ($\mathbf{u}\cdot\mathbf{e}_r = 0$) will we need to reintroduce Ekman circulation. This fact implies that dissipation in the interior of the fluid will dominate dissipation in boundary layers at the scale of the convective flow, and justifies the approximation mentioned above.

Equation (3) will be re-written in the following manner, which highlights its formal analogy with the beta-plane equation used in geophysical fluid dynamics (Pedlosky, 1987):

$$\frac{\mathrm{d}\Lambda}{\mathrm{d}t} = \nabla^2\omega + Ra\frac{\partial T}{\partial\theta}, \tag{4}$$

we define Λ as the potential vorticity:

$$\Lambda = \omega - \frac{2}{E}\ln L.$$

Let $\tilde{u}(r)$ and $\tilde{T}(r)$ be time-averaged standard deviations for the convective velocity and temperature fluctuation, and $\delta(r)$ be the mean, time-averaged vortex size, as functions of the cylindrical radius. In order to derive scaling relationships, we identify two steps in the process of the evolution of the vorticity field.

First, the thermal instability produces lateral gradients of temperature, and this results in the creation of vorticity. For instance, one rising plume gives birth to a cyclone on its prograde side, and an anticyclone on its retrograde side. We therefore write

$$\frac{\mathrm{d}\omega}{\mathrm{d}t} \sim Ra\frac{\partial T}{\partial\theta} \tag{5}$$

The fundamental assumption of this analysis is that later in time, structures of high Re_l evolve at constant potential vorticity. Under the influence of advection by rising and falling radial currents, they exchange vorticity with the planetary vorticity field $2\ln L/E$:

$$\frac{\mathrm{d}\Lambda}{\mathrm{d}t} = 0 \Rightarrow \frac{\mathrm{d}\omega}{\mathrm{d}t} \sim E^{-1}\frac{2}{L}\frac{\mathrm{d}L}{\mathrm{d}r}\mathbf{u}\cdot\mathbf{e}_r \tag{6}$$

The timescale of these phenomena is the vortex turnover time t:

$$t \sim 1/\omega \sim \delta/\tilde{u} \tag{7}$$

On this timescale, structures of high Re_l are indeed immune to viscosity, and therefore do not lose potential vorticity. This inertial balance thus assumes that under the influence of radial advection (Reynolds stresses), transfer of energy occurs between the convective scale and the scale of energy dissipation (this will be made more precise, see below).

This results in a three-term balance

$$(5),(6) \text{ and } (7) \quad \Rightarrow \quad \frac{\tilde{u}^2}{\delta^2} \sim \frac{Ra\, r\tilde{T}}{\delta} \sim E^{-1}\frac{2}{L}\frac{\mathrm{d}L}{\mathrm{d}r}\tilde{u}. \tag{8}$$

One needs another equation to solve for $\tilde{u}$,$\tilde{T}$ and δ. It is provided by the Nusselt number, which is the ratio of the total heat flux Q_{tot} over the conductive heat flux:

$$Nu = \frac{Q_{tot}}{Q_{conv}} = 1 + \overline{uT}P^2.$$

Since lateral temperature gradients create radial velocity, we assume that $\tilde{u}$ and $\tilde{T}$ are correlated, and therefore we approximate $\overline{uT}$ by $\tilde{u}\tilde{T}$. In the limit of high departures from criticality Ra/Ra_c, we write:

$$Nu \sim 1 + \tilde{u}\tilde{T}P^2 \sim \tilde{u}\tilde{T}P^2. \tag{9}$$

Solving (8) and (9) for the three variables yields the set of inertial scaling relations:

$$\left.\begin{aligned} \tilde{u} &\sim \left(r^{2/5}f(r)^{1/5}\right)\ \left(\frac{Ra_Q}{P^2}\right)^{2/5} E^{1/5} \\ \delta &\sim \left(r^{1/5}f(r)^{3/5}\right)\ \left(\frac{Ra_Q}{P^2}\right)^{1/5} E^{3/5} \\ \tilde{T} &\sim \left(r^{-2/5}f(r)^{-1/5}\right)\ Nu\left(Ra_Q P^3\right)^{-2/5} E^{-1/5} \end{aligned}\right| \quad f(r) = \left(\frac{2}{L}\frac{\mathrm{d}L}{\mathrm{d}r}\right)^{-1} = \frac{r_e^2 - r^2}{2r} \tag{10}$$

where $Ra_Q = Ra \cdot Nu$ is the heat-flux based Rayleigh number. These relations draw their interest from the fact that they depend on geophysically well-constrained parameters. The set of equations (10) has been written by Cardin and Olson (1994), and has been found to be in qualitative agreement with their experiments. It is interesting to note that in this inertial scaling, diffusion constants ν and κ do not play a role in the expressions for $\tilde{u}$ and δ (Christensen, 2001). This becomes clear when time is re-scaled using the container rotation time Ω^{-1} instead of the viscous diffusion time. Let starred variables $\tilde{u}^* = \tilde{u}E$ (which is the Rossby number), $\delta^* = \delta$, $\tilde{T}^* = \tilde{T}$ be the variables in the new scaling. There appears a parameter $\gamma = Ra_Q E^3 P^{-2}$, which is independent of either diffusion constant. These constants only play a role in the scaling for $\tilde{T}^*$, and the scaling relations write (dropping the r-dependence):

$$\left.\begin{aligned} \tilde{u}^* &\sim \gamma^{2/5} \\ \delta^* &\sim \gamma^{1/5} \\ \tilde{T}^* P E^{-1} &\sim \gamma^{-2/5} \end{aligned}\right| \quad \gamma = \frac{\alpha g Q_{tot}}{\rho C_p \Omega^3 D^2} \tag{11}$$

We now return to the original definition of the non-dimensional time, since we will also be interested in viscous effects. The previous scaling relations have indeed been derived in the limit of high Reynolds numbers and high departures from criticality. We investigate now the case when viscous effects are important, i.e. lower Reynolds numbers. We expect then that the conservation of potential vorticity will hold only on timescales of order of the viscous diffusion time, and (7) is replaced with:

$$\frac{\mathrm{d}\omega}{\mathrm{d}t} \sim \nabla^2\omega \Rightarrow t \sim \delta^2 \tag{12}$$

This yields another three-term balance:

$$(5),(6) \text{ and } (12) \quad \Rightarrow \quad \frac{\tilde{u}}{\delta^3} = \frac{Ra\, r\tilde{T}}{\delta} = E^{-1}\frac{2}{L}\frac{\mathrm{d}L}{\mathrm{d}r}\tilde{u}. \tag{13}$$

Solving (13) and (9) for the three variables yields the set of viscous scaling relations:

$$\begin{aligned}
&\tilde{u} \sim \left(r^{1/2} f(r)^{1/3}\right) \left(\frac{Ra_Q}{P^2}\right)^{1/2} E^{1/3} \\
&\delta \sim \left(f(r)^{1/3}\right) \; E^{1/3} \\
&\tilde{T} \sim \left(r^{-1/2} f(r)^{-1/3}\right) \; Nu \left(Ra_Q P^3\right)^{-1/2} E^{-1/3}
\end{aligned} \tag{14}$$

The radial dependence of equations (10) and (14) predicts that velocity and vortex size must decrease at increasing radius, due to the influence of the increasing slope of the spherical boundary. This is the fundamental effect of the spherical geometry, and it is in qualitative agreement with the radial profiles shown on figure 6. We now factor out the r-dependence and turn to the scaling of variables picked up at r_{max}.

For quantitative validation by laboratory experiments some adaptations towards moderate Ra/Ra_c are necessary. In that case, Ra_c has to be substracted from Ra since it represents a part of buoyancy unavailable for generation of motion. The scaling parameter therefore has to be $Ra - Ra_c$ instead of Ra. The rest of the analysis above is valid if $Nu - 1$ replaces Nu. Moreover, in order to convert Ra into Ra_Q, we need an estimate of Nu, since it is not measured in our experiments. The exact relationship is not crucial however, since variations of $Nu - 1$ are not dramatic when compared to those of $Ra/Ra_c - 1$. For experiments done in water, Sumita and Olson (2000) have obtained $Nu \sim (Ra/Ra_c)^{1/2}$ in the parameter range we use, a value in agreement with calculations of Tilgner and Busse (1997) with $P = 10$. For the water case we will use this relation. For experiments done in liquid gallium, since the departure from criticality is not high, we will use a constant Nusselt number.

Figure 10 presents the test of a viscous, and inertial balance on the radial velocity data. While the inertial scaling adequately fits the data for both liquids, the viscous scaling is accurate only for experiments in water up to a value of Ra/Ra_c of order 10, and inaccurate for experiments in gallium. These conclusions are confirmed when we scale the mean of the radial cell size distribution, using the results for δ (Figure 11). A viscous scaling adequately describes the evolution of $\overline{\delta_r}$ in water, where, once the E dependance has been removed, no significant increase is observed with Ra/Ra_c. Only an inertial scaling can describe the increase of $\overline{\delta_r}$ with Ra/Ra_c in liquid gallium. However, this test is less significant than the previous one, because of the broadness of cell size distribution, and the low dynamics (less than one decade) of its variations. The evolution of the temperature fluctuations with the parameters (not shown) is also in good agreement with the predictions of the inertial model.

At the scale of the convection flow, the QG model with no dissipation at the spherical external boundary is thus accurate. Kinetic energy created by buoyancy is partly dissipated in water (inertial and viscous terms are of the same order of magnitude), and little dissipation takes place in gallium. One efficient dissipative mechanism of kinetic energy remains available in this latter case: zonal flow is not subject to any forced vertical circulation that prevents friction on the external boundary. We therefore suspect that kinetic energy is transported from the scale of convective flow to the scale of the container through Reynolds stresses.

An equation for the time-averaged zonal velocity $\overline{u_\theta}$ can be deduced by averaging the θ-component of equation (1):

$$\overline{(\mathbf{u} \cdot \nabla)\, u_\theta} + 2E^{-1} \mathbf{e}_z \times \overline{\mathbf{u}} \cdot \mathbf{e}_\theta = -E^{-1} \overline{\nabla \Pi \cdot \mathbf{e}_\theta} + \nabla^2 \overline{u_\theta}.$$

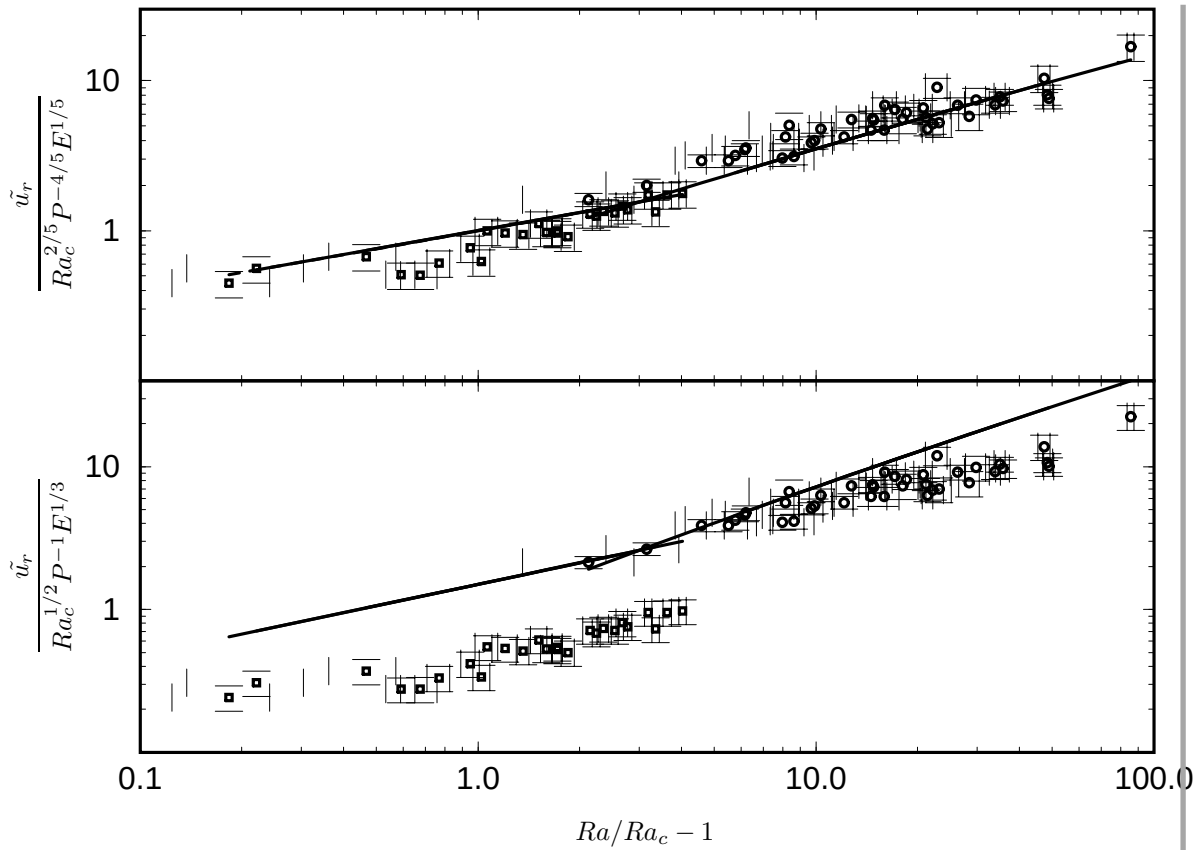

Figure 10: Reduced radial velocity for gallium (squares) and water (circles) experiments. Up: test of the inertial balance. Black line in water corresponds to theoretical dependence $y \sim ((Nu-1)(Ra/Ra_c-1))^{2/5}$ with $Nu \sim (Ra/Ra_c)^{1/2}$. Black line in gallium corresponds to dependence $y \sim (Ra/Ra_c-1)^{2/5}$. Scaling prefactor is 1. Low: test of the viscous balance. Black line in water is $y \sim ((Nu-1)(Ra/Ra_c-1))^{1/2}$, and in gallium $y \sim (Ra/Ra_c-1)^{1/2}$. Prefactor is 1.5 .

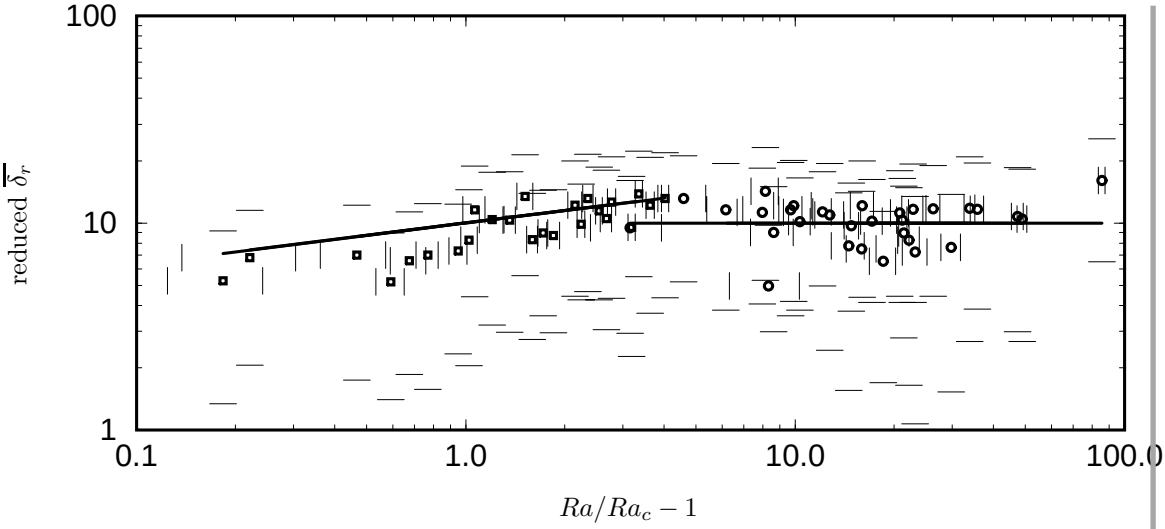

Figure 11: Reduced cell size for gallium (squares) and water (circles) experiments. The viscous scaling is tested for water experiments, the reduced cell size is therefore $\overline{\delta_r}/E^{1/3}$. The inertial scaling is tested for gallium experiments, the reduced cell size is therefore $\overline{\delta_r}/(Ra_Q^{1/5}P^{-2/5}E^{3/5})$. Black line in gallium corresponds to dependence $y \sim (Ra/Ra_c - 1)^{1/5}$. Black line in water is $y \sim 1$. Both prefactors are 10.

If we assume ergodicity, which seems to be realized by zonal flow, and identify the time-average with the θ-average, then $\overline{\nabla\Pi \cdot \mathbf{e}_\theta}$ identically vanishes. We also have

$$2E^{-1}\mathbf{e}_z \times \overline{\mathbf{u}} \cdot \mathbf{e}_\theta = 2E^{-1}\overline{u_r}.$$

$\overline{u_r}$ can be expressed through the Ekman circulation formula (Greenspan, 1968):

$$\overline{u_r} = \frac{E^{1/2}}{2L\sqrt{\mathbf{n}\cdot\mathbf{e_z}}}\overline{u_\theta}$$

Where $\mathbf{n}$ is the normal to the spherical boundary. The time averaged θ-component of equation (1) finally writes:

$$\overline{(\mathbf{u}\cdot\nabla)\,u_\theta} + \frac{E^{-1/2}}{L\sqrt{\mathbf{n}\cdot\mathbf{e_z}}}\overline{u_\theta} = \nabla^2\overline{u_\theta}. \tag{15}$$

Far from the inner cylinder, Ekman friction dominates dissipation in the interior of the fluid and equilibrates with Reynolds stresses. Closer to the inner cylinder, a passive boundary layer can set up where the viscous drag from the interior of the fluid equilibrates Ekman friction. Therefore the predominant source of energy is Reynolds stresses, and the predominant sink of energy is Ekman friction on the outer boundary. This is the behavior of a large-gap configuration, and would not be true in a small-gap case (Plaut and Busse, 2001). The balance, from which we factor out, as usual, the r-dependence, writes:

$$\overline{u_r\frac{\partial u_\theta}{\partial r}} \sim \frac{E^{-1/2}}{L\sqrt{\mathbf{n}\cdot\mathbf{e_z}}}\overline{u_\theta} \quad \Rightarrow \quad \frac{\tilde{u}^2}{\overline{\delta_r}} \sim \frac{\overline{u_\theta}}{E^{1/2}}. \tag{16}$$

The nonvanishing nonlinear coupling term is indeed the $r\theta$ component of Reynolds stress, and it has been estimated as $\tilde{u}^2/\overline{\delta_r}$, assuming that a constant degree of correlation exists between u_r and u_θ over the range covered by experiments. A justification

for this can be found in the principle of potential vorticity conservation: due to this principle, rising currents have a tendancy to turn into anticyclones. The excess of negative vorticity induces a retrograde zonal circulation which is well correlated with the radial flow. This interpretation also predicts that the energy contained into the zonal flow cannot be significantly higher than the energy contained into the radial flow. The degree of correlation has therefore to decrease as the zonal flow becomes too high.

Variations of $\overline{\delta_r}$ with controlling parameters are not very significant in the range of experiments ($\overline{\delta_r}$ is always of order 1), and therefore we keep $\overline{\delta_r} \sim 1$ in equation (16). Since zonal flow results from inertial effects, inertial scaling has to be adopted for $\tilde{u}$. The resulting formula writes:

$$\overline{u_\theta} \sim \left(\frac{Ra_Q}{P^2}\right)^{4/5} E^{9/10}. \tag{17}$$

This scaling is tested on figure 12, and yields a prefactor 1. Only data points corresponding to sufficiently developed convection are kept. The data for $\overline{u_\theta}$ are more scattered than for $\tilde{u_r}$, but the agreement with equation (17) is still good. This test highlights the importance of Ekman layers near the spherical boundary for the determination of zonal flow.

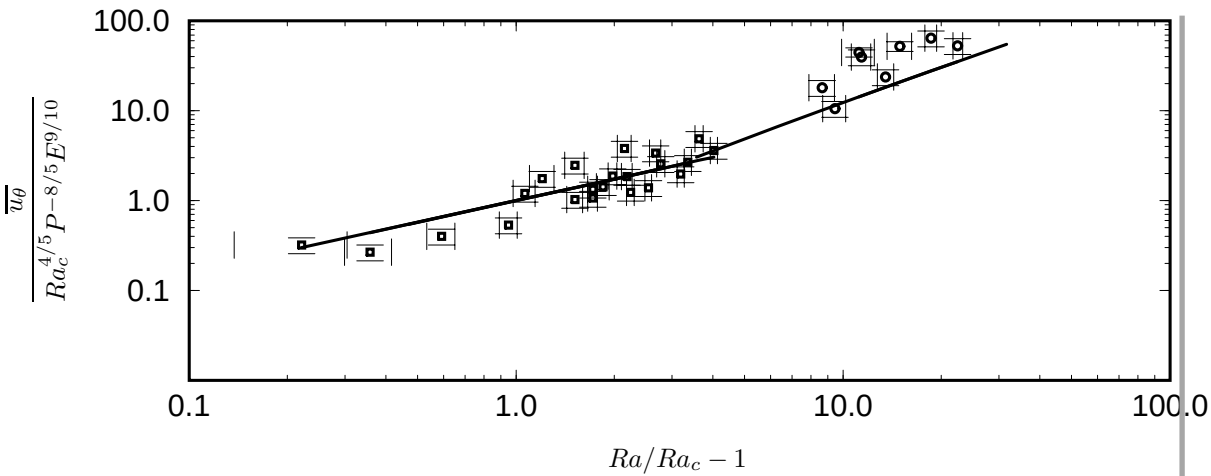

Figure 12: Reduced zonal flow velocity. Black line is $y \sim ((Nu-1)(Ra/Ra_c-1))^{4/5}$ in water and $y \sim (Ra/Ra_c-1)^{4/5}$ in gallium. Scaling prefactor is 1.

This last point clearly shows the adequation of an interpretation of zonal flow in terms of Reynolds stresses. Zonal velocities observed in water are not important, because kinetic energy is partly dissipated at the convective scale. In gallium they take part in the only efficient dissipative mechanism left, and this explains their rapid growth as the convective instability injects more energy into the system.

A condition for the inertial regime can be established, by comparing the orders of magnitude of dissipation through Ekman friction of the zonal flow, and dissipation at the convective scale. The former can be estimated as $\overline{u_\theta}^2/E^{1/2}$ and the latter as $\tilde{u}^2/\delta^2$. Either inertial or viscous scaling predicts that δ is not smaller than $E^{1/3}$ and therefore the condition writes:

$$\frac{\overline{u_\theta}^2}{\tilde{u}^2} > E^{1/6}$$

and this yields (the fractional power of E is approximated for simplification):

$$\frac{Ra_Q}{P^2}E^{3/2} > 1 \tag{18}$$

Equation (18) is satisfied by gallium experiments, for which left-hand side of (18) is at least 30. For water experiments this term is of order 10^{-2} for experiments at $E = 9.7\ 10^{-6}$ near the onset, and reaches values of order 1 for the more supercritical experiments at $E = 2.4\ 10^{-6}$. This confirms that the inertial regime is attained only for the lower E experiments in water, and for all experiments in gallium.

Having proposed a mechanism for the zonal velocities, we come back to an interpretation of the measurements of $\overline{\Delta t}$, the average time between zeros of the radial velocity profiles, in terms of the average azimuthal size of the vortices $\overline{\delta_\theta}$. We have

$$\overline{\delta_\theta} = 2\overline{u_\theta}\overline{\Delta t}.$$

The factor 2 is used because $\overline{\Delta t}$, as it is defined, describes half a period. $\overline{\delta_\theta}$ is plotted on figure 13, with error bars corresponding to the standard deviation of lateral size distribution. Here zonal flow velocity is determined using theoretical scaling relations. Therefore only data points corresponding to sufficiently developped flows have been kept. Horizontal lines are predicted sizes of vortices at convection onset. Here again, the scaling proposed for δ in the previous section correctly describes the order of magnitude and variations of $\overline{\delta_\theta}$ within the error bars, and the increase in size predicted by the inertial scaling is effective only for high Re_l experiments. An aspect ratio δ_r/δ_θ can be estimated, and is of order 1 at high Re_l (compare figure 13 with the third graph in figure 8). In the inertial regime, cells generally tend to grow with increasing Ra/Ra_c, and can become larger than cells at convection onset.

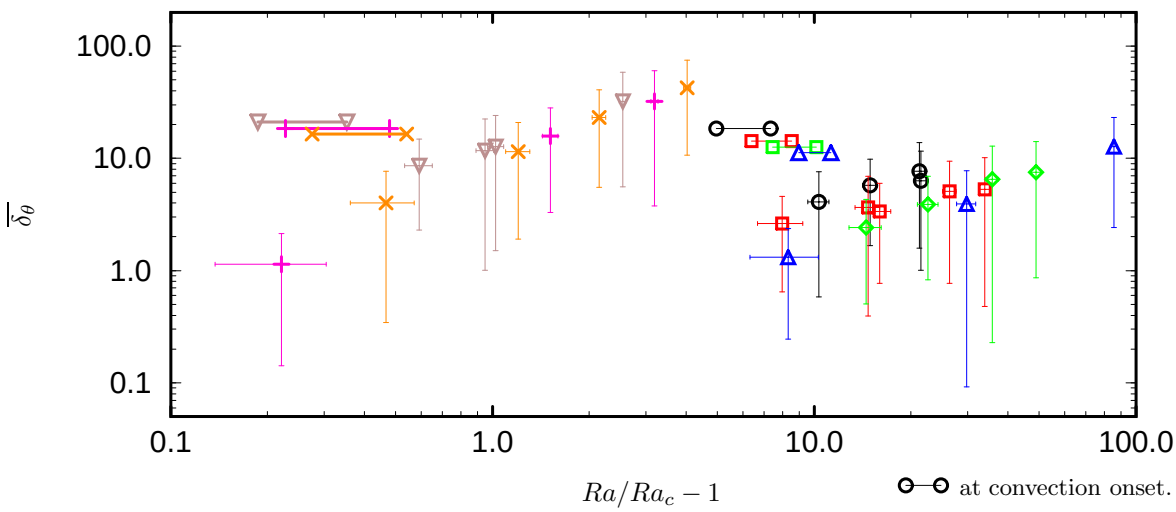

Figure 13: Lateral size of vortices at radius r_{max}, near the inner cylinder.

7 Discussion

We have shown that thermal convection in water and gallium exhibits properties that can well be accounted for by the inertial model we have derived. The use of two

liquids with very different Prandtl numbers was essential to discriminate between the inertial and the viscous models.

Our measurements enable us to show that the typical local Reynolds number is much larger in the gallium experiments than in water. The most striking consequence of these high Reynolds numbers for gallium is the apparition of large zonal velocities, well explained by Reynolds stresses in the framework of our inertial model. By combining the expression for the local Reynolds number

$$Re_l = \tilde{u}\overline{\delta_r} \sim \left(\frac{Ra_Q}{P^2}\right)^{3/5} E^{4/5},$$

and those for the zonal and convective velocities, we obtain

$$\overline{u_\theta}/\tilde{u_r} \sim Re_l^{2/3} E^{1/6}.$$

As expected, this ratio is controlled almost entirely by the Reynolds number. The 2/3 slope is in good agreement with the data (dashed line in figure 9).

We emphasize that, in the inertial regime, there is no efficient dissipation mechanism at convective scale, and therefore kinetic energy created by buoyancy has to cascade to larger scales where dissipation takes place by shear of zonal flow on boundaries. The energy flow towards large scales is the classical mechanism invoked in 2D turbulence. While in a plane layer, this mechanism leads to the apparition of structures as large as the container (Sommeria, 1986), in the spherical geometry only zonal motions are permitted at this scale. The large zonal velocities we measure in gallium are reminiscent of the observations of Grote et al. (2000) for a numerical model of convection with a stress-free outer boundary. These authors report a strong intermittency as the zonal flow tends to wipe out the convective structures from which it draws its strength. In our experiments, we found no evidence for this mechanism. It is probably due to the fact that zonal velocities in our case are limited by friction on the Ekman layers of the outer boundary, while only viscosity in the interior of the shell can control the amplitude of the zonal flow in the numerical model.

The adequation of an explanation of experiments based on the model by Cardin and Olson (1994) reasserts the interest of a two-dimensional approach. However, their model did not take Ekman friction of zonal flow on the external boundary into account. This represents an easy improvement, after which it will be possible to compare convective structures determined numerically and experimentally. Using more ultrasonic transducers, it should be possible indeed to construct a local map of convective structures, and investigate the radial and zonal geometry of convective vortices.

Our results also bear some relevance to the geodynamo problem. Recent numerical models (Christensen et al., 1998) have shown that dynamo action can take place in a spherical shell when thermal convection is only a few times critical. The mechanism is of α^2-type, meaning that the conversion of poloidal to toroidal magnetic field, and vice-versa, is done by vortices at the convective scale. In the Earth, it is believed that the conversion of poloidal to toroidal field is due to an ω effect, i.e. zonal flow. Our observations suggest that for sufficiently low Ekman numbers and high Reynolds numbers, this zonal flow will be naturally produced by the convective engine.

Although all these results apply to a non-magnetic case, we think it is of some interest to extrapolate them to the parameters of the core. We use $E = 10^{-14}$ and

Variable	Value
Re_l	10^6
Re	10^8
$\tilde{u}$	10^{-3} m/s
$\overline{\delta_r}, \overline{\delta_\theta}$	10 km
$\overline{u_\theta}$	10^{-2} m/s

Table 5: Values for the Earth's core deduced from inertial scaling.

$P = 1$, both estimated using parameters in table 2. The heat-flux based Rayleigh number can be expressed as:

$$Ra_Q = \frac{\alpha g Q_{tot} D^2}{k \kappa \nu}.$$

From an upper bound for the total heat flux emerging at the Core- Mantle Boundary (CMB) $Q_{tot} = 10$ TW (Labrosse et al., 1997), we infer $Ra_Q = 10^{30}$. The condition (18) for the inertial regime is satisfied, and therefore the inertial scaling is chosen to derive the core estimates of convective velocity, cell size, Reynolds number and zonal flow which are summarized in table 5. The local Reynolds number is very high and indicates a strongly turbulent state. The global Reynolds number is of the same order of magnitude as the estimate made in the introduction. Convective flow velocities (10^{-3} m/s) are ten times larger than CMB estimates, of order 10^{-4} m/s (Hulot et al., 1990), obtained from secular variations of the magnetic field. The ratio of zonal over convective velocity yields the value 10, while estimates based on geophysical observations (Jault et al., 1988) lead to zonal velocities lower than convective velocities. As we have seen in the scaling analysis, this ratio is very likely to saturate at a value of order 1 (Christensen, 2001), even though we have not observed it. A too strong zonal flow would indeed suppress convection by mixing plumes. Developed QG turbulence should favor large structures, but still the influence of vortex stretching results in very small typical cell sizes.

The kind of flow described by these parameters would not be very efficient in maintaining a magnetic field: the essential part of kinetic energy, which is in zonal flow, is lost for dynamo action. The first effects of the addition of a magnetic field on this configuration would be to enlarge structures and slow down velocities, especially zonal velocity (Brito et al., 1995). This will be checked in future experiments in the presence of an azimuthal magnetic field.

Acknowledgments.

We are grateful to D. Jault for sharing his valuable theoretical knowledge on rotating thermal convection. We also thank U. Christensen and an anonymous referee for helpful comments on this paper. This work was supported by program *Expérimentation* of CNRS/INSU, by the Région Rhône-Alpes and by the Université Joseph Fourier.

Appendix: Notes on experiments and data processing.

Experimental procedure.

For the acquisition of one experimental record, the sphere is spun up to the desired speed, and the thermal regulation system is then turned on and tuned to the desired gradient. Then we wait until spin-up is complete (3 mn), until thermal equilibrium is reached at boundaries (10 mn), until convection pattern is statistically stationary (depends on the departure from criticality, but typically 30 mn). Then recording is started.

Structure and resolution of recordings.

One velocity profile is a set of 224 (water) and 130 (gallium) velocity points covering a distance of respectively 83.6 and 92.8 mm. The effective resolution is therefore 0.37 mm (water) and 0.71 mm (gallium). In fact the real resolution is lower because one ultrasonic burst is composed of eight cycles. The Doppler apparatus then overlaps measurement windows of respective sizes $0.37 \times 8 = 2.96$ mm and $0.71 \times 8 = 5.68$ mm, to recover the aforementioned effective resolution. Some care has been taken on this point in figures 6 and 7, where squares denote real measurement points, and the solid line represents the profile obtained at effective resolution.

$N = 4096$ complete radial velocity profiles are acquired, at a sampling rate between 6 and 18 profiles per second. This represents roughly one tenth of the viscous dissipation time D^2/ν. The actual time resolution is lower because of averaging for noise reduction. Typical averaging is done over 10 profiles, using a median filter, and this lowers the time step to some 0.5 seconds. Also recorded meanwhile are 4096 complete velocity profiles on the lateral probe.

Temperature perturbation signals are recorded at a sample rate of 3 to 6 samples per second. The imposed temperature gradient is recorded using thermo-resistive platinum probes. The temperature gradient has to be corrected by some 15 percent temperature drop in lexan when experimenting with water.

Extracted scalar data and error bars.

Scalars are extracted from filtered signals. Let N be the number of profiles, and $u_i(r)$ an individual profile. The mean velocity is

$$\overline{u}(r) = \frac{1}{N} \sum_i u_i(r),$$

and the standard deviation of velocity

$$\tilde{u}(r) = \sqrt{\frac{1}{N} \sum_i \left(u_i(r) - \overline{u}(r)\right)^2}.$$

Error bars on $\tilde{u_r}$ and $\overline{u_\theta}$ account for the reproductibility of measurements, and of

the uncertainty due to seeding particles centrifugation (see retrieval of zonal flow). Error bars on $\overline{\delta_r}$, $\overline{\delta_\theta}$ and $\overline{\Delta t}$ are the standard deviations $\tilde{\delta_r}$, $\tilde{\delta_\theta}$ and $\tilde{\Delta t}$ of the size distributions. An example histogram of size distribution is shown on figure 14.

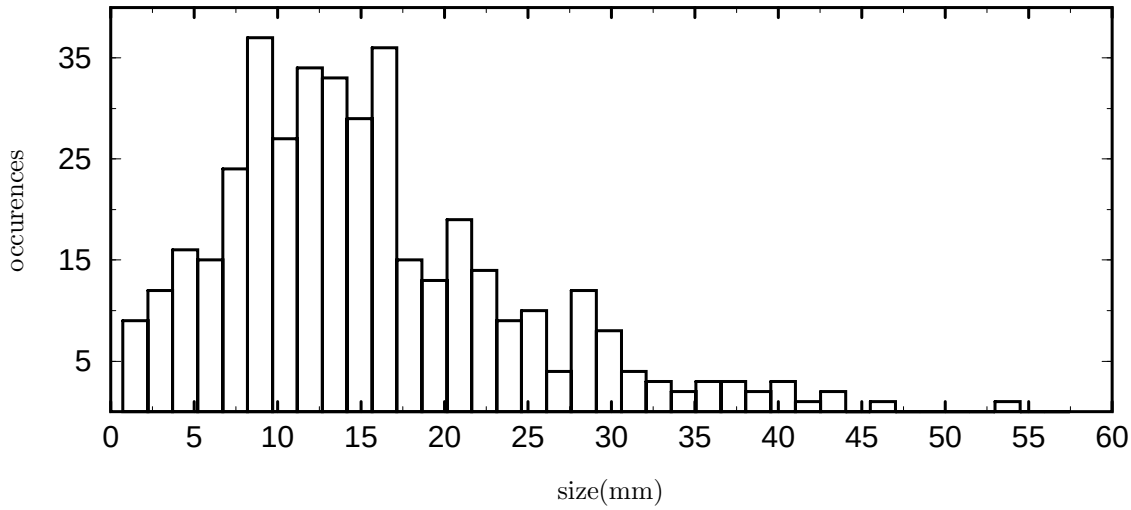

Figure 14: Histogram of the distribution of radial cell sizes in the convective flow, measured at radius 60 mm in water, for experiment of figure 4.3 (Ekman number is 4.8 10^{-6}, Rayleigh number is 26.6 times critical).

Retrieval of mean zonal flow velocity.

The mean velocity $\overline{u}_{mes}$ measured on the lateral probe can be expressed in the system of local axes of figure 2 as a function of mean radial and zonal flow velocities $\overline{u_r}$ and $\overline{u_\theta}$:

$$\overline{u}_{mes} = \overline{u_r}\cos(\alpha+\theta) + \overline{u_\theta}\sin(\alpha+\theta).$$

The convention of positive radial velocity directed inwards has been used here. Hence

$$\overline{u_\theta} = \frac{\overline{u}_{mes}}{\sin(\alpha+\theta)} - \overline{u_r}\cot(\alpha+\theta).$$

For a purely convective flow $\overline{u_r}$ averages out. In the case of the experiment some care has to be taken on this point, since $\overline{u_r}$ is slightly different from zero due to centrifugation/centripetation of seeding particles. Therefore it has to be corrected here.

The unknown is the angle θ. if r denotes the distance on the lateral probe since the beam entered the fluid, and R the radius of the fluid sphere, some algebra yields:

$$\sin\theta = \frac{\sin\alpha}{\sqrt{1 - 2\cos\alpha\dfrac{R}{r} + \left(\dfrac{R}{r}\right)^2}}$$

α remains to be determined. The beam enters the solid sphere at an angle 40^o

Medium	v_P (m/s)
water	1500 (at 20^o C)
liq. gallium	[a] 2873 (at 30^o C)
lexan	[b] 2340 ± 190
copper	[b] 5040 ± 350

Table 6: Compressional ultrasonic wave velocities v_P in media used in the experiment. [a]: Beyer and Ring (1972); [b]: this study.

and is then refracted at the liquid interface such that:

$$\sin(\alpha) = \frac{v_P(liq)}{v_P(sol)} \sin(40^o)$$

where v_P stands for the compressional ultrasonic wave velocity of the considered media. Using the values listed in table 6, this gives $\alpha = 24.3 \pm 1.5^o$ for experiments in water, and $\alpha = 21.5 \pm 1.5^o$ in gallium. This corresponds to a minimal distance to inner cylinder of $d = 5 \pm 3$ mm in water and $d = 1 \pm 3$ mm in gallium. The uncertainties are of the same importance as the size of the Doppler measurement volume, and they affect the horizontal position of plots in figure 7.

References

Ardes, M., Busse, F. H., and Wicht, J., Thermal convection in rotating spherical shells, *Phys. Earth Planet. Int.*, *99*, 55–67, 1997. 3

Aurnou, J. M. and Olson, P., Rotating magnetoconvection experiments in liquid gallium, *J. Fluid Mech.*, *430*, 283–307, 2001. 4

Beyer, R. T. and Ring, E. M., *Liquid metals: chemistry and physics*, Marcel Dekker, N.Y., 1972. 32

Brito, D., Cardin, P., Nataf, H.-C., and Marolleau, G., Experimental study of a geostrophic vortex of gallium in a transverse magnetic field, *Phys. Earth Planet. Int.*, *91*, 77–98, 1995. 4, 29

Brito, D., Nataf, H.-C., Cardin, P., Aubert, J., and Masson, J., Ultrasonic Doppler velocimetry in liquid gallium, in press, *Experiments In Fluids*, 2001. 7

Busse, F. H., Thermal instabilities in rapidly rotating systems, *J. Fluid Mech.*, *44*, 441–460, 1970. 2, 10, 20

Busse, F. H. and Carrigan, C. R., Laboratory simulation of thermal convection in rotating planets and stars, *Science*, *191*, 81–83, 1976a. 3

Busse, F. H. and Carrigan, C. R., Convection induced by centrifugal buoyancy, *J. Fluid Mech.*, *62*, 579–592, 1976b. 3, 5

Cardin, P. and Olson, P., An experimental approach of thermo-chemical convection in the Earth's core, *Geophys. Res. Let.*, *19*, 1995–1998, 1992. 3

Cardin, P. and Olson, P., Chaotic thermal convection in a rapidly rotating spherical shell: consequences for flow in the outer core, *Phys. Earth Planet. Int.*, *82*, 235–239, 1994. 3, 4, 17, 20, 21, 22, 28

Carrigan, C. R. and Busse, F. H., An experimental and theoretical investigation of the onset of convection in rotating spherical shells, *J. Fluid Mech.*, *126*, 287–305, 1983. 3

Chamberlain, J. A. and Carrigan, C. R., An experimental investigation of convection in a rotating sphere subject to time-varying thermal boundary conditions, *Geophys. Astrophys. Fluid Dyn.*, *8*, 303–327, 1986. 3

Chandrasekhar, S., *Hydrodynamic and Hydromagnetic Stability*, Clarendon, Oxford, 1961. 4

Christensen, U., Olson, P., and Glatzmaier, G. A., A dynamo model interpretation of geomagnetic field structures, *Geophys. Res. Let.*, *25*, 1565–1568, 1998. 28

Christensen, U. R., Excitation of zonal flow by deep convection in the major planets, poster Communication at European Geophysical Society, 2001. 22, 29

Christensen, U. R., Aubert, J., Busse, F. H., Cardin, P., Dormy, E., Gibbons, S., Glatzmaier, G. A., Honkura, Y., Jones, C. A., Kono, M., Matsushima, M., Sakuraba, A., Takahashi, F., Tilgner, A., Wicht, J., and Zhang, K., A numerical dynamo benchmark, *Submitted to Phys. Earth. Plan. Int.*, 2001. 9

Cordero, S., Experiments of convection in a rotating hemispherical shell: transition to chaos, *Geophys. Res. Let.*, *20*, 2587–2590, 1993. 3

Cordero, S. and Busse, F. H., Experiments of convection in a rotating hemispherical shell: transition to a quasi periodic state, *Geophys. Res. Let.*, *19*, 733–736, 1992. 17

Dormy, E., Cardin, P., and Jault, D., MHD flow in a slightly differentially rotating spherical shell, with conducting inner core, in a dipolar magnetic field, *Earth Plan. Sci. Let.*, *160*, 15–30, 1998. 9

Glatzmaier, G. A. and Olson, P., Highly supercritical thermal convection in a rotating spherical shell: centrifugal vs. radial gravitiy, *Geophys. Astrophys. Fluid Dyn.*, *70*, 113–136, 1993. 5

Glatzmaier, G. A. and Roberts, P. H., A three dimensional self consistent computer simulation of the geomagnetic field reversal, *Nature*, *377*, 203–209, 1995. 4

Greenspan, H. P., *The theory of rotating fluids*, Breukelen Press, 1968. 25

Grote, E., Busse, F. H., and Tilgner, A., Regular and chaotic spherical dynamos, *Phys. Earth Planet. Int.*, *117*, 259–272, 2000. 3, 28

Hulot, G., Le Mouël, J.-L., and Jault, D., The flow at the Core-Mantle boundary: symmetry properties, *J. Geomag. Geoelectr.*, *42*, 857–874, 1990. 29

Jault, D., Gire, C., and Le Mouël, J. L., Westward drift, core motions and exchanges of angular momentum between core and mantle, *Nature*, *333*, 353–356, 1988. 20, 29

Jones, C. A., Convection-driven geodynamo models, *Phil. Trans. R. Soc. Lond. A*, *358*, 873–897, 2000. 4

Jones, C. A., Soward, A. M., and Mussa, A. I., The onset of thermal convection in a rapidly rotating sphere, *J. Fluid Mech.*, *405*, 157–179, 2000. 3

Labrosse, S., Poirier, J. P., and Le Mouel, J. L., On cooling of the earth's core, *Phys. Earth Planet. Int.*, *99*, 1–17, 1997. 29

Okada, K. and Ozoe, H., Transient responses of natural convection heat transfer with liquid gallium under an external magnetic field in either the x, y, or z direction, *Ind. Eng. Chem. Res.*, *31*, 700–706, 1992. 2

Pedlosky, J., *Geophysical fluid dynamics*, Springer, New-York, 1987. 21

Plaut, E. and Busse, F. H., Low prandtl number convection in a rotating cylindrical annulus., *Submitted to J. Fluid. Mech.*, 2001. 25

Roberts, P. H., On the thermal instability of a self gravitating fluid sphere containing heat sources, *Philos. Trans. R. Soc. London, Ser. A*, *263*, 93–117, 1968. 2

Sabot, J.-L. and Lauvray, H., Gallium and gallium compounds, in *Encyclopedia of Chemical technology*, vol. 12, pp. 299–317, Kirk-Othmer, 1995. 2

Sommeria, J., Experimental study of the two-dimensional inverse energy cascade in a square box, *J. Fluid Mech.*, *170*, 139–168, 1986. 28

Stacey, F. D., *Physics of the Earth*, Brookfield Press, 1992. 2

Sumita, I. and Olson, P., Laboratory experiments on high Rayleigh number thermal convection in a rapidly rotating hemispherical shell, *Phys. Earth Planet. Int.*, *117*, 153–170, 2000. 3, 4, 17, 23

Sun, Z. P., Schubert, G., and Glatzmaier, G. A., Transition to chaotic thermal convection in a rapidly rotating sphericall shell, *Geophys. Astrophys. Fluid Dyn.*, *69*, 95–131, 1993. 3

Takeda, Y., Velocity profiles measurements by ultrasonic doppler shift method, *Int. J. Heat Fluid Flow*, *8*, 313–, 1986. 7

Tilgner, A. and Busse, F. H., Finite amplitude convection in rotating spherical fluid shells, *J. Fluid Mech.*, *332*, 359–376, 1997. 3, 23

Zhang, K., Spiralling columnar convection in rapidly rotating spherical shells, *J. Fluid Mech.*, *236*, 535–556, 1992. 3

Zhang, K. and Gubbins, D., Scale disparities and magnetohydrodynamics in the Earth's core, *Phil. Trans. R. Soc. Lond. A*, *358*, 899–920, 2000. 4